Ceramics International 52 (2026) 26100–26117

Contents lists available at ScienceDirect

Ceramics International

journal homepage: www.elsevier.com/locate/ceramint

Influence of deposition temperature on the microstructure, wear and corrosion behaviour of AlTiN/AlTiCrN ceramic coatings on A8 tool steel

Musa Muhammed [a,*], Mousa Javidani [a,**], Majid Heidari [b], Tom Levasseur [b], Mohammad Jahazi [c]

[a] Department of Applied Science, University of Quebec at Chicoutimi, Saguenay, QC, G7H 2B1, Canada
[b] DK SPEC Company, 1060, Chemin Olivier, St-Nicolas, Québec, QC, G7A 2M8, Canada
[c] Department of Mechanical Engineering, École de Technologie Supérieure (ETS), Montreal, QC, H3C 1K3, Canada

ARTICLE INFO

Keywords:
Deposition temperature
AlTiN/AlTiCrN
Cathodic arc evaporation
Physical vapour deposition
Wear
Corrosion

ABSTRACT

Deposition temperature is a known pivotal process parameter influencing the tribological and corrosion performance of physical vapour deposited ceramic coatings. Yet, the impact of the parameter remains highly system-specific, limiting generalization of observed trends across different coating-substrate systems. Therefore, this study investigates the effect of deposition temperature (350 – 450 °C; designated as T350 – T450) on the microstructural evolution, mechanical properties, wear, and corrosion behaviour of AlTiN/AlTiCrN coatings deposited on AISI A8 tool steel for woodworking applications. Coatings were characterized using scanning electron microscopy, energy dispersive X-ray spectroscopy, X-ray diffraction, nanoindentation, scratch testing, ASTM G65 abrasive wear testing, and electrochemical analysis. Results showed that T350 exhibited the lowest wear rate (~2 × 10^{-4} mm^3/Nm); 36 and 56 % lower than T400 and T450, respectively. This superior wear resistance was attributed to its higher adhesion (critical load ~ 11 N), thicker coating (2.8 μm), smoother surface (R_a = 0.25 μm), and higher H/E ratio (0.072), despite an intermediate hardness (31 GPa). Although maximum hardness (36 GPa) occurred at T400 due to finer crystallite (~10.4 nm) and elevated microstrain (0.77 %), its higher macroparticle density (0.18 particle/μm^2) and roughness (R_a = 0.31 μm) compromised performance. Additionally, corrosion resistance was superior at T350 and T450 (protective efficiency >45 % and porosity <0.70 %), attributed to denser structures, thicker coatings, coarser crystallites, and higher chromium content. Overall, these findings demonstrate that a deposition temperature of 350 °C provides an optimal balance of wear and corrosion resistance in AlTiN/AlTiCrN-coated A8 tool steels, offering valuable insights for tailoring PVD process parameters for woodworking applications.

1. Introduction

AISI A8 tool steel is widely used for manufacturing wood-cutting tools such as saw blades due to its cost-effectiveness and its favourable combination of toughness and wear resistance, which are essential for resisting chipping and mechanical failure during repetitive wood sawing operations. However, despite its good bulk mechanical properties, A8 tool steel alone may not provide sufficient hardness and wear resistance under the highly abrasive and elevated-temperature conditions encountered during wood cutting [1], [2]. To address these limitations, layered AlTiN/AlTiCrN coatings have emerged as promising protective candidates. The multilayer architecture enhances crack deflection and load distribution across the coating interfaces, thereby improving resistance to crack propagation and coating failure during cyclic cutting loads. In addition, the quaternary AlTiCrN component contributes to improved hardness, oxidation resistance, and chemical stability compared with conventional ternary nitride coatings. Collectively, the combination of a tough and cost-effective A8 tool steel substrate with a hard, thermally stable, and oxidation-resistant AlTiN/AlTiCrN ceramic coating, therefore, creates a synergistic system capable of withstanding severe abrasive wear and elevated service temperatures typical of industrial wood sawing applications [1], [3], [4]. Although the performance of these coatings is influenced by their multilayer architecture [5] and the condition of the underlying substrate [6], process

* Corresponding author.
** Corresponding author.
E-mail addresses: mmuhammed@etu.uqac.ca (M. Muhammed), mjavidan@uqac.ca (M. Javidani).

https://doi.org/10.1016/j.ceramint.2026.04.059
Received 23 January 2026; Received in revised form 23 March 2026; Accepted 5 April 2026
Available online 8 April 2026

parameters during cathodic arc deposition also play a crucial role in determining coating properties and overall functional behaviour. Among these parameters, deposition temperature is particularly important because it directly affects adatom mobility, phase formation, residual stress development, and microstructural evolution during film growth, which ultimately influence the mechanical and tribological performance of the coating [7]. In this context, the following paragraphs provide insights into how variations in deposition temperature influence the wear and corrosion behaviour of ceramic coatings.

Several studies have demonstrated that deposition temperature exerts a complex and often coating/system-dependent influence on the tribological performance of PVD ceramic coatings. For instance, Ling et al. [8] reported that increasing the deposition temperature of AlCrN coatings on tungsten carbide from 250 to 450 °C resulted in lower wear rates. The improvement in wear resistance was attributed to enhanced coating hardness, thickness, and adhesion strength at elevated temperatures. Similarly, Gautier and Machet [9] observed improved wear resistance of Cr coatings on stainless steel with increasing deposition temperature (250 – 500 °C), attributing the improvement to the annihilation of lattice defects and consequent hardness enhancement. Meanwhile, contrasting observations were reported by Warcholinski et al. [10] for a similar AlCrN coating investigated by Ling et al. [8], but on HS6-5-2 steel substrate. The authors reported a decline in hardness and adhesion strength of AlCrN coatings with increasing deposition temperature from 350 to 450 °C. These deteriorations in hardness and adhesion strength were linked to crystallite growth coupled with the compressive residual stress relaxation at higher temperatures [2], [10]. Collectively, the findings from these studies suggest that the influence of deposition temperature on the tribological performance of ceramic coatings is largely dependent on the coating-substrate system.

In addition to the tribological aspects, deposition temperature has also been shown to significantly affect the corrosion behaviour of PVD ceramic coatings. For example, Persson et al. [11] investigated the corrosion resistance of CrN-coated H13 tool steel and found that increasing the deposition temperature from 230 to 430 °C reduced the coating defect density and increased coating thickness. Consequently, electrolyte penetration and localized pitting became limited, culminating in improved corrosion performance. However, about a decade later, Valleti et al. [12] reported a contrasting finding for CrN coating on high-speed steel, as increasing the deposition temperature (230 – 500 °C) deteriorated the corrosion resistance. This occurrence was correlated with the accompanying reduction in the Cr phase content and the increase in the defect density (including pinholes and macroparticles) at elevated temperature. More recently, Taweesup et al. [13] reported enhanced corrosion resistance of TiCrN coatings deposited on an H13 tool steel with increasing temperatures from 25 to 190 °C, attributed to reduced coating porosity, leading to improved coating densification. Nonetheless, these seemingly contradictory findings underscore that the effect of deposition temperature on the corrosion performance of ceramic coatings is, much like the tribological behaviour, i.e., system-specific and influenced by the complex interplay between the coating chemistry and substrate composition.

Overall, the foregoing discussion highlights the system-specific influence of deposition temperature, thereby rendering the direct generalization across different coating-substrate systems difficult. Notably, a critical literature survey reveals the absence of systematic studies examining the influence of deposition temperature on the wear and corrosion behaviour of AlTiN/AlTiCrN multilayer coatings deposited on A8 tool steel. This gap is particularly significant given the widespread industrial application of A8 tool steel in woodworking tools, where components are simultaneously subjected to abrasive wear and corrosive environments. To address this knowledge gap, this study systematically investigates how varying deposition temperature influences the microstructural, morphological, and mechanical properties of AlTiN/AlTiCrN coatings on A8 tool steel, and how these temperature-induced modifications translate into wear and corrosion performance. The novelty of this work lies in establishing direct correlations between deposition temperature, microstructural evolution, and the tribological–corrosion response of AlTiN/AlTiCrN coating; a technologically relevant multilayer ceramic coating system. By elucidating the governing mechanisms that control hardness, adhesion, defect development, and durability, this study advances the understanding of temperature-dependent growth processes in nitride-based ceramic coatings. Therefore, the findings provide valuable insights into process-microstructure-performance relationships in AlTiN/AlTiCrN ceramic coatings, directly aligning with the scope of Ceramics International, which emphasizes fundamental understanding and performance enhancement of engineered ceramic materials for demanding applications.

2. Experimental details

2.1. Substrate preparation and coating deposition

The chemical composition of the AISI A8 tool steel substrate obtained using optical emission spectroscopy (SPECTROMAXx, LMX10) is presented in Table 1.

The substrates with dimensions 75 mm × 25 mm × 10 mm were ground to achieve an average roughness (R_a) of ~0.1 μm (T350 = 0.101 ± 0.009 μm, T400 = 0.100 ± 0.009 μm, T450 = 0.100 ± 0.008 μm), then cleaned sequentially using a mild alkaline detergent (deconex, Borer Chemie AG), rinsed with water, and dried under vacuum. The coatings were deposited using a cathodic arc evaporation system, the mechanism of which is schematically represented in Fig. 1a. The system is equipped with planar targets including pure Cr as well as hybrid compositions of $Al_{67}Ti_{33}$ and $Al_{50}Ti_{50}$. The deposition process involved loading the prepared substrates into the deposition chamber at a distance of 18 – 20 cm from the targets, followed by evacuation to a vacuum to minimize coating contamination and enhance deposition efficiency [14]. This was followed by Al/Ti ion etching and a subsequent argon gas etch to remove any residual surface contaminants. During the etching process, for instance, metal ion etching, a high-speed plasma composed of Al and Ti metal ions, is directed toward the substrate, which is maintained at a strong negative bias (350 –750 V), for approximately 20 min. This process promotes the removal of surface contaminants through sputtering and simultaneously activates a superficial layer on the substrate's surface [15]. The AlTiN/AlTiCrN coatings were then deposited following established procedures and parameters in our previous studies [3], with the deposition temperature varied between 350, 400, and 450 °C, which were designated as T350, T400, and T450, respectively. The AlTiN base layer was deposited for 40 – 46 min while the AlTiCrN layer was deposited for 60 – 69 min. Continuous substrate rotation was maintained throughout the process to ensure uniformity during deposition [2]. After deposition, the system was cooled before unloading the samples for subsequent characterization. Fig. 1b shows a schematic of the AlTiN/AlTiCrN coating.

2.2. Coating characterization

The surface morphology and coating cross-section were analyzed using a scanning electron microscope (SEM, JSM-6480LV, Japan). Thereafter, quantitative post-imaging analysis for Macroparticle (MP) density, size, and coating thickness was carried out using Image J software [16]. For the MP analysis, 10 SEM micrographs of consistent magnification and contrast were evaluated, while 10 measurements were recorded for coating thickness determination. The surface roughness was measured using a stylus-based profilometer (Mahr MahrSurf PS

Table 1
Chemical composition of the AISI A8 tool steel substrate (wt. %).

C	Cr	Mo	W	Si	Mn	Fe
0.5	8.1	1.2	1.1	0.8	0.4	Balance

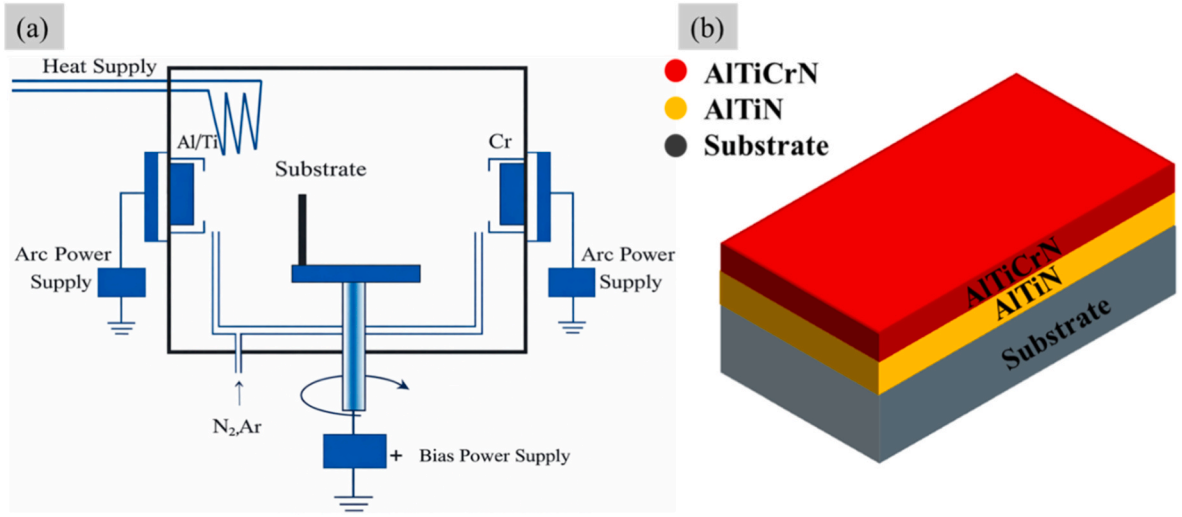

Fig. 1. (a) Schematic illustration of the cathodic arc evaporation process and (b) Schematic showing the AlTiN/AlTiCrN coating deposited on the AISI A8 tool steel substrate.

10, Germany), with each reported value representing the average of 10 measurements for each condition. The elemental composition of the coatings was examined by energy dispersive X-ray spectroscopy (EDS, INCA energy 250). The phase composition was characterized by X-ray diffraction (XRD, D8 Discover, Bruker AXS, Germany) utilizing Co kα radiation. Data were collected at a step size of 0.05° with a counting time of 0.5 s/step, at an accelerating voltage of 45 kV and tube current of 40 mA.

Nanoindentation tests (Anton Paar MCT3) were performed to measure the hardness and elastic modulus of the coatings under a maximum load of 20 mN, with a loading rate of 40 mN/min, a dwell time of 2 s, and an unloading rate of 40 mN/min. A minimum of five indents were obtained for each condition. Adhesion strength was determined using a progressive load scratch test (Anton Paar MCT3) with a Rockwell-type diamond stylus of 50 μm radius. The load increased linearly from 0 to 30 N during the test. The loading rate, scratch speed, and track length were 20.98 N/min, 3.5 mm/min, and 5 mm, respectively. Each test was repeated three times per coating condition. The wear resistance was evaluated following ASTM G65, procedure B, based on the mass loss method [3]. The test operates under a three-body abrasion mechanism, in which the coated specimen, silica sand particles, and rubber wheel simulate the cutting tool, entrained wood debris and contaminants, and the wooden workpiece, respectively. During testing, the fixed sample is subjected to sustained abrasive action from silica sand particles while being forced into contact with a chlorobutyl rubber wheel [17]. Each test condition was repeated three times, and the resulting wear volume was corrected to account for rubber wheel wear using Equation (1) [2]:

$$\textit{Adjusted wear volume}\ (mm^3) = \textit{wear volume}\ (mm^3) \times \frac{228.6\ mm}{\textit{Wheel diameter after test}\ (mm)} \quad (1)$$

thereafter, the adjusted wear volumes were used in the computation of the wear rates [18]. Post-wear examination of the wear tracks was also performed using SEM-EDS to identify the dominant wear mechanisms. Cross-sectional analysis of the wear track was performed using an optical microscope (Nikon Eclipse ME600, Japan) to determine the wear track depth and width.

The corrosion performance was assessed using a potentiostat (PGZ 100 VoltaLab) interfaced with VoltaMaster software. The test cell included an Ag/AgCl reference electrode, a platinum counter electrode, and the coated specimen (1 cm^2 exposed area) immersed in a 3.5 wt% NaCl solution. Prior to measurements, the system stabilized at Open Circuit Potential (OCP) for approximately 3600 s. The electrochemical impedance spectroscopy (EIS) was performed by applying an AC signal over the 100 kHz - 100 mHz frequency range at the OCP. Potentiodynamic polarization (PDP) tests were then carried out within the potential window of – 0.25 to + 1 V at a scan rate of 2 mV/s. The corrosion potential (E_{corr}), corrosion current density (i_{corr}), and polarization resistance (R_p) were determined using the Tafel extrapolation technique. In this method, the linear portions of the anodic and cathodic branches of the potentiodynamic polarization curve, plotted as potential versus the logarithm of current density, are extrapolated back to their intersection point. The intersection of these extrapolated lines corresponds to the E_{corr} and i_{corr}. Subsequently, the R_p is calculated from the slope of the potential-current relationship using the Stern-Geary equation, which relates R_p to the Tafel slopes and i_{corr} [19]. All electrochemical measurements were repeated three times for each condition to ensure the reproducibility and reliability of the obtained results. The coating porosity (P) was calculated using Equation (2) [20]:

$$P\ (\%) = \frac{R_{ps}}{R_{pc}} \times 10^{-\left(\frac{|\Delta E_{corr}|}{B_a}\right)} \quad \text{Equation 2}$$

where R_{ps} and R_{pc} are the polarization resistances of the substrate and coating, respectively; ΔE_{corr} is the potential difference between the coated sample and substrate; and B_a is the anodic Tafel slope.

The protective efficiency (PE) was determined using Equation (3) [21]:

$$PE\ (\%) = \left(1 - \frac{i_{corr(coating)}}{i_{corr(substrate)}}\right) \times 100 \quad \text{Equation 3}$$

here, $i_{corr(coating)}$ and $i_{corr(substrate)}$ denote the corrosion current densities of the coated and uncoated substrates, respectively.

3. Results

3.1. Microstructural evaluation

3.1.1. Effect of deposition temperature on surface characteristics

Fig. 2a–c presents the micrograph showing the surface morphology of the AlTiN/AlTiCrN coatings. The surface of the coated tool steels is characterized by deposition defects, namely, macroparticles (MPs) and craters. These defects are typical for PVD coatings, and a lot of research is ongoing on the subject, due to their detrimental impact on the quality and performance of the coatings [4]. The MPs may result from a

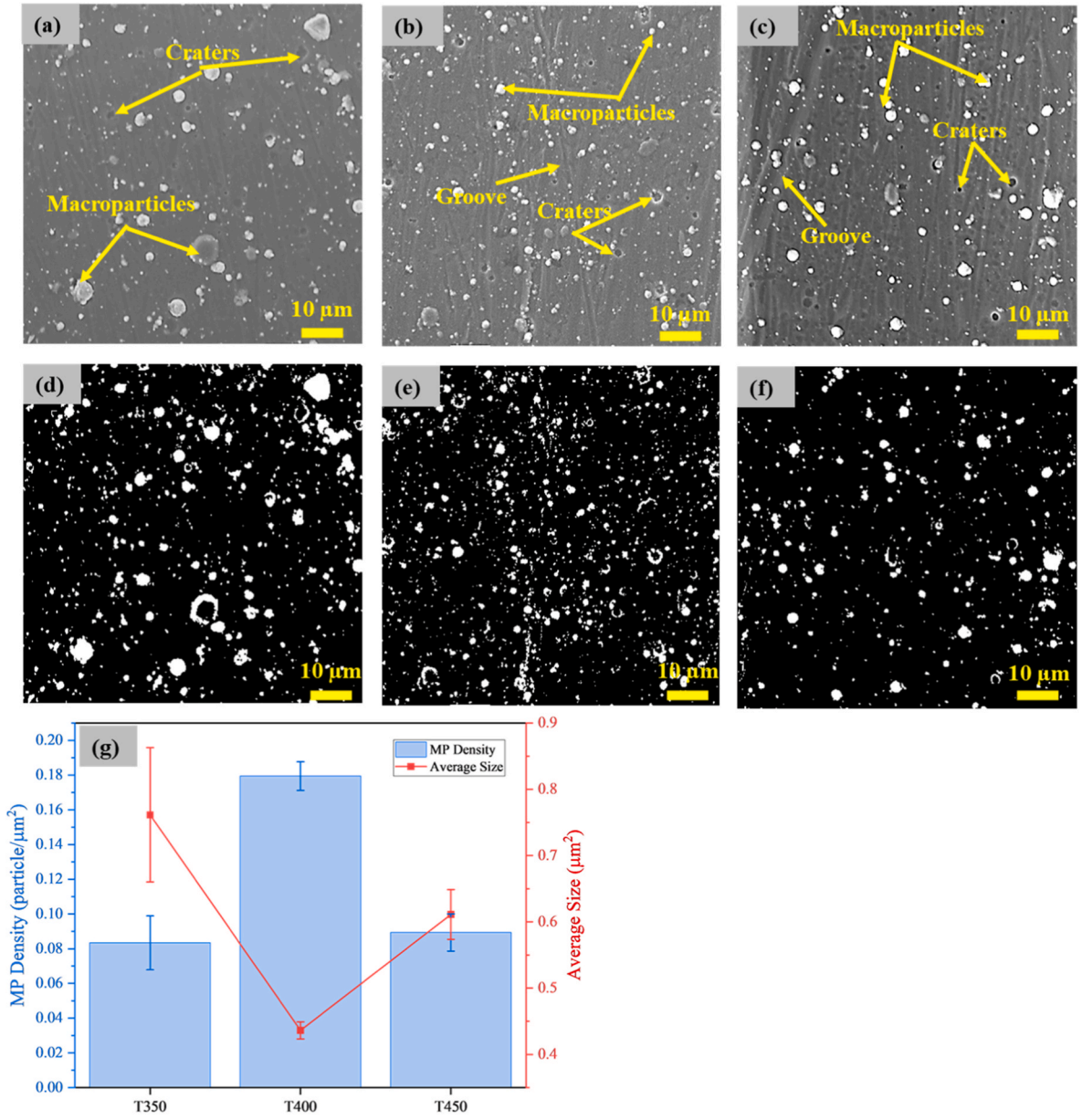

Fig. 2. Surface SEM micrographs and corresponding ImageJ-processed images of AlTiN/AlTiCrN-coated AISI A8 tool steel deposited at different temperatures: (a, d) 350 °C; (b, e) 400 °C; and (c, f) 450 °C; (g) Quantitative analysis of macroparticle density and average macroparticle size as a function of deposition temperature.

combined effect of hydrodynamic effects and thermal shock on the target, leading to the ejection of molten particles, which eventually solidify on the substrate as MPs. The craters, on the other hand, may arise from incomplete reactions between the coating species and the reactive gas (N_2) and often become evident following the flaking of loosely adhered MPs [3]. Further examination revealed the presence of profiling grooves from substrate preparation, highlighting the significant role of the substrate topography on the morphology of the deposited coatings [15]. More so, the grooves appear to be more visible with increasing deposition temperature, with the coatings deposited at 400 and 450 °C (Fig. 2b and c) exhibiting the most pronounced grooves. This could suggest a reduction in coating thickness with increasing deposition temperature, as substrate irregularities are expected to be more prominent in thinner coatings [14].

Fig. 2d–f presents the ImageJ-processed micrographs, which were used for the MP quantification. The relationship between the MP statistics and deposition temperature presents a novel finding, as it has not been explored in previous studies [8], [22]. The result of the analysis is presented in Fig. 2g. The figure reveals that the MPs reached a maximum MP density of about 0.18 particle/μm^2 at T400. In contrast, the T350 and T450 conditions exhibited comparable MP densities around 0.09 particle/μm^2 (with T450 being slightly higher), representing about 50 % reduction compared to T400. Meanwhile, the average MP size was generally higher at T350 (about 0.75 μm^2), followed by about 43 and 17 % reductions with increasing temperature at T400 and T450, respectively.

The evolution of the MPs with deposition temperature could be explained by considering MP agglomeration-coalescence and bombardment-resputtering mechanisms, as illustrated in Fig. 3. Explicitly, at a relatively low deposition temperature of 350 °C, the impact of the MPs is less effective, which reduces their ability to bombard and interrupt the surface diffusion and rearrangement of previously condensed particles [23]. This reduced disruption of the condensed MPs, favors MP agglomeration and subsequent coalescence, producing fewer MPs with larger sizes, as observed in the T350 condition. When the temperature increases to 400 °C, the diffusion of incoming MPs is

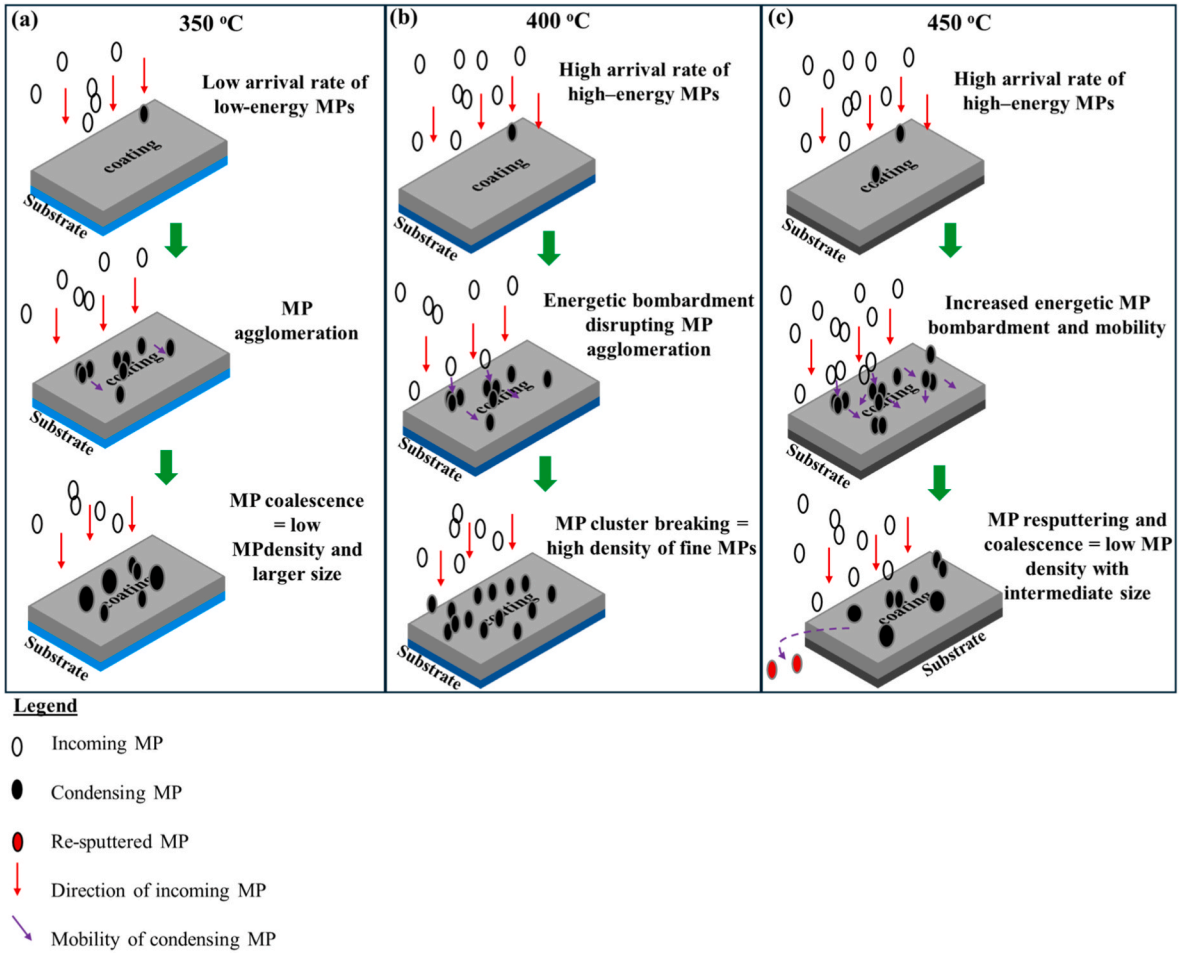

Fig. 3. Schematic illustration of macroparticle evolution mechanisms at different deposition temperatures for AlTiN/AlTiCrN coating.

enhanced, leading to a higher arrival rate on the substrate surface. However, the enhanced bombardment of the incoming particles disrupts agglomeration and coalescence, thereby producing a higher MP density but with smaller particle sizes. Upon further increasing the temperature to 450 °C, the arrival rate of the MPs is further increased, but the accompanying increased energetic bombardment, leading to resputtering, decreases the MP density compared to T400. Nonetheless, the higher particle mobility at this temperature (i.e., T450) could facilitate the coalescence of the remaining MPs, resulting in an increase in average MP size relative to T400 [2], [14]. The proposed interpretation is consistent with classical descriptions of macroparticle formation, transport, and interaction with the growing film in cathodic arc deposition, as reported in the foundational works of Boxman [24] and Anders [25]. In summary, the MPs are generally larger at 350 °C due to the dominance of MP agglomeration-coalescence, while the highest MP density with the least size occurs at 400 °C due to the influence of MP bombardment interrupting coalescence. Meanwhile, at 450 °C, MP density decreases, but the size increases relative to 400 °C, attributed to

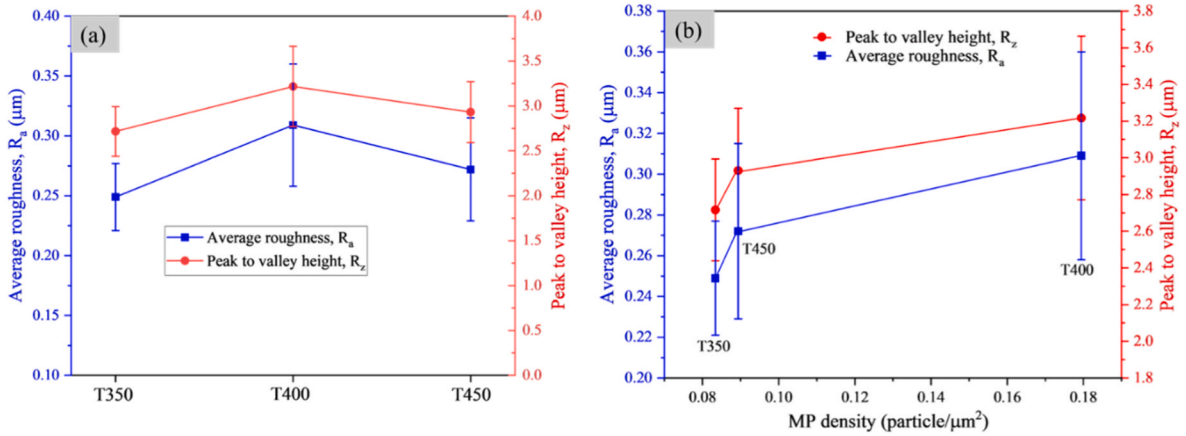

Fig. 4. (a) Surface roughness parameters (R_a and R_z) and (b) correlation between R_a and R_z and macroparticle density of AlTiN/AlTiCrN coatings deposited at different temperatures.

the combined effects of resputtering and enhanced MP mobility promoting coalescence.

Fig. 4a presents the surface roughness parameters (R_a and R_z) of the coatings deposited at different temperatures. R_a denotes the arithmetic mean surface roughness, while R_z represents the peak-to-valley height. Together, these parameters are widely used to characterize the surface roughness of PVD coatings [2]. From the figure, both parameters exhibit a similar trend, suggesting a consistent evolution of the overall surface topography with deposition temperature. For instance, the R_a increases from 0.25 μm (T350) to 0.31 μm (T400), followed by a reduction to 0.27 μm (T450). Notably, the roughness values obtained in this study are relatively higher than those reported for other AlTiCrN-based coatings [26], primarily due to the comparatively rougher substrate condition (R_a ~0.1 μm) prior to deposition. Moreover, previous studies have shown that substrate topography significantly influences the roughness of the deposited coatings [15]. Nonetheless, the coating roughness evolution with deposition temperature could be correlated with the MP statistics. As shown in Fig. 4b, R_a and R_z exhibit a positive correlation with MP density. For instance, the increase in MP density from T350 to T450 coincides with higher R_a and R_z values, while the reduction in MP density from T400 to T450 corresponds to lower R_a and R_z values. Consequently, the relatively higher roughness of the T400 condition could, therefore, be explained by its maximum MP density. In this regard, the accumulation of MP defects increases surface asperities, thereby producing a rougher coating surface [3]. In summary, although the roughness did not follow a distinct trend with temperature, it shows a clear correlation with the MP density, with the highest roughness values at T400 attributed to its highest MP density.

3.1.2. *Effect of deposition temperature on cross-sectional morphology, thickness, and elemental composition*

Fig. 5 shows the cross-sectional morphology of the AlTiN/AlTiCrN coatings deposited at the three investigated temperatures. From the figure, overall, the coatings exhibit a dense structure and minimal visible defects. The coating thickness is also observed to reduce progressively with increasing deposition temperature. Explicitly, the thickness was found to be 2.8 μm at 350 °C, followed by 4 % and 14 % reductions upon increasing the temperature to 400 and 450 °C, respectively. These values fall within the range (2 – 4 μm) typically reported for AlTiN/AlTiCrN coatings under similar deposition conditions [3], [15]. Moreover, comparable trends have also been reported by Warcholinski et al. [10], who observed about a 20 % reduction in AlCrN coating thickness with increasing temperature from 350 to 450 °C.

In this regard, the reduction in the deposition rate leading to lower coating thickness with increasing temperature could be explained by two phenomena: ion bombardment-resputtering mechanism and the so-called “target poisoning”. With respect to the ion-bombardment mechanism, at higher deposition temperatures, the incoming coating adatoms exhibit higher mobility, leading to more energetic bombardment of the substrate. Consequently, this leads to an increased tendency of adatom resputtering, thereby reducing the deposition rate (from 0.0236 to 0.0202 μm/min) and resulting in 14 % thinner coatings, as observed in the T450 condition [3]. Meanwhile, according to the target poisoning phenomenon, at elevated temperatures, there is an increased tendency for the formation of compound metallic nitrides on the surface of the targets, leading to target poisoning. These metallic nitrides formed on the targets reduce the effective evaporation of coating adatoms from arc spots, thereby reducing deposition rate, leading to thinner coatings [10].

Further examination of the coating cross-sectional morphology reveals a bilayer structure, comprising a darker AlTiN base layer and a brighter AlTiCrN top layer. This morphology is consistent with previous findings by Danek et al. [27], who reported brighter contrast in Cr-rich AlTiCrN coatings. The EDX elemental mapping of the coating shown in Fig. 6a confirms the presence of Al, Ti, Cr, and N in the top AlTiCrN layer, while the AlTiN base layer contains Al, Ti, and N, along with traces of Cr. The EDX line scan (Fig. 6b) suggests that the trace Cr detected in the AlTiN base layer likely originates from interdiffusion of Cr from the AlTiCrN top layer or from the Cr-containing substrate. This effect becomes more pronounced at higher deposition temperatures (T400 and T450), as evidenced by the increased Cr content (See Table 2). This trend could be attributed to enhanced atomic mobility at elevated temperatures, which facilitates interdiffusion across the coating-substrate and interlayer boundaries [2].

Additionally, the EDX compositional results shown in Table 2 further reveal that the coatings exhibit stoichiometric compositions at all deposition temperatures, indicated by an N/(Al + Ti + Cr) ratio greater than 1. This suggests that there is a supply of reactive N_2 gas to promote the formation of stable metallic nitrides [8], [28]. Furthermore, researchers have observed a correlation between higher ratios of Al/(Al + Ti + Cr) and improved tribological performance of PVD coatings [29]. In this study, for the AlTiN layer, the Al/(Al + Ti + Cr) ratio decreases with temperature from 0.56 at T350 to 0.51 at T450 conditions. However, much lower values of the ratios were observed for the AlTiCrN layer (0.39 to 0.41), which can be explained by the substitution of Al atoms with Cr atoms in the AlTiCrN layer [3]. Nonetheless, the bilayer architecture could benefit from the contributions of both layers to enhance the functional performance of the coating. Overall, considering both layers cumulatively, the deposition temperature appears not to have a significant effect on the Al/(Al + Ti + Cr) ratio, with average values generally in the range of 0.46 – 0.48. In summary, increasing the deposition temperature resulted in: (1) a reduction in coating thickness, (2) coatings with generally stoichiometric compositions, and (3) no significant variation in the Al/(Al + Ti + Cr) ratio.

3.1.3. *Effect of deposition temperature on phase composition, crystallite size, and microstrain*

Fig. 7a shows the XRD profiles of the AlTiN/AlTiCrN coatings deposited at different temperatures. In the figure, dashed lines are used to indicate reference peak positions according to the Crystallography Open Database [30]. The diffraction peaks presented by the coated samples consist of contributions from both the coating and the substrate. Specifically, three substrate peaks at $2\theta = 52.2°$, 77°, and 99.4° were identified based on the reference code 96-901-3474. With an increase in deposition temperature (from T350 to T450), an increase in the intensity of the main substrate peak ($2\theta = 52.2°$) was observed. This observation is an indication of a reduction in the coating thickness at higher

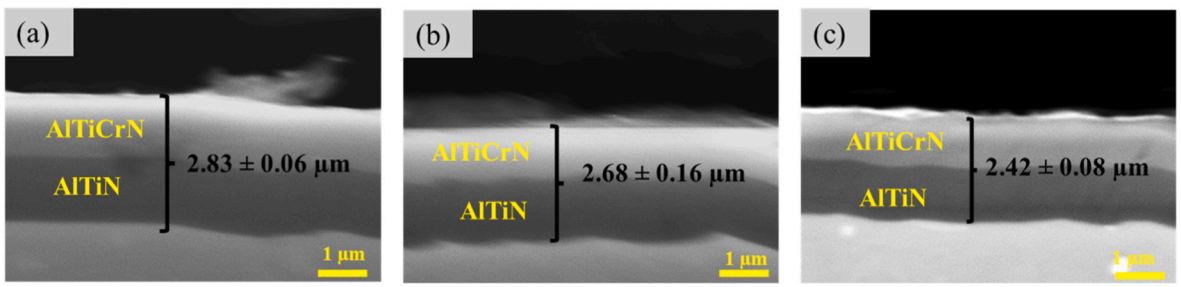

Fig. 5. Cross-sectional SEM micrographs of AlTiN/AlTiCrN coatings deposited on tool steel substrate at temperatures of: (a) 350 °C; (b) 400 °C; (c) 450 °C.

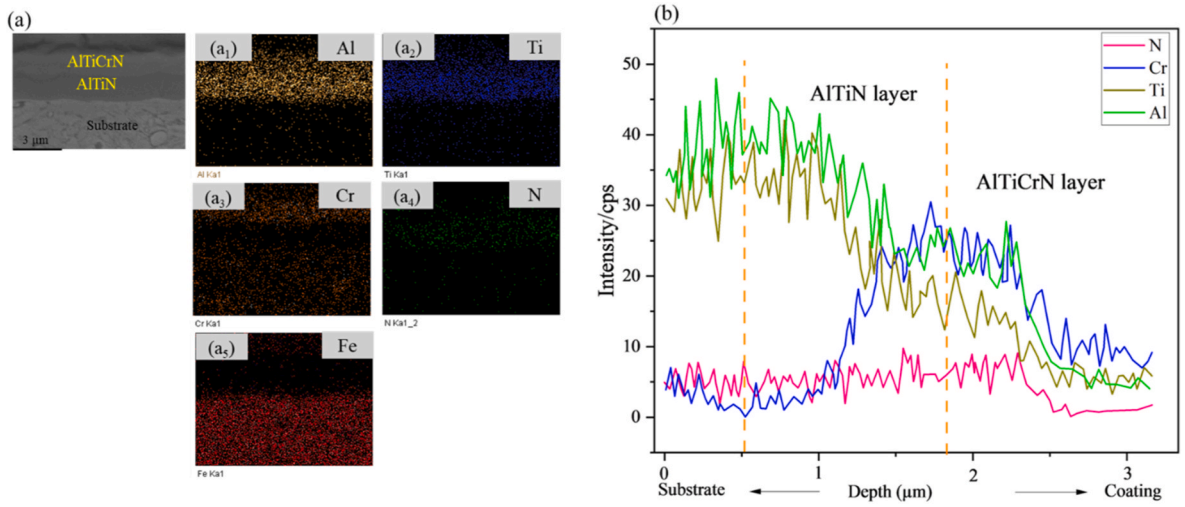

Fig. 6. (a) EDX elemental mapping and (b) corresponding line scan profile of the AlTiN/AlTiCrN coating deposited at 350 °C.

Table 2
EDX elemental composition of the AlTiN/AlTiCrN coatings deposited at different temperatures.

Layer	Condition	Composition (at. %)				$\frac{[Al]}{[Al]+[Ti]+[Cr]}$	$\frac{[N]}{[Al]+[Ti]+[Cr]}$
		Al	Ti	Cr	N		
AlTiN	T350	27.40	20.70	1.20	50.70	0.56	1.03
	T400	25.70	20.80	2.10	51.50	0.53	1.06
	T450	24.30	20.70	2.50	52.50	0.51	1.11
AlTiCrN	T350	16.70	8.60	18.0	56.70	0.39	1.31
	T400	21.0	12.30	15.60	51.20	0.43	1.05
	T450	20.60	12.20	17.10	50.20	0.41	1.01

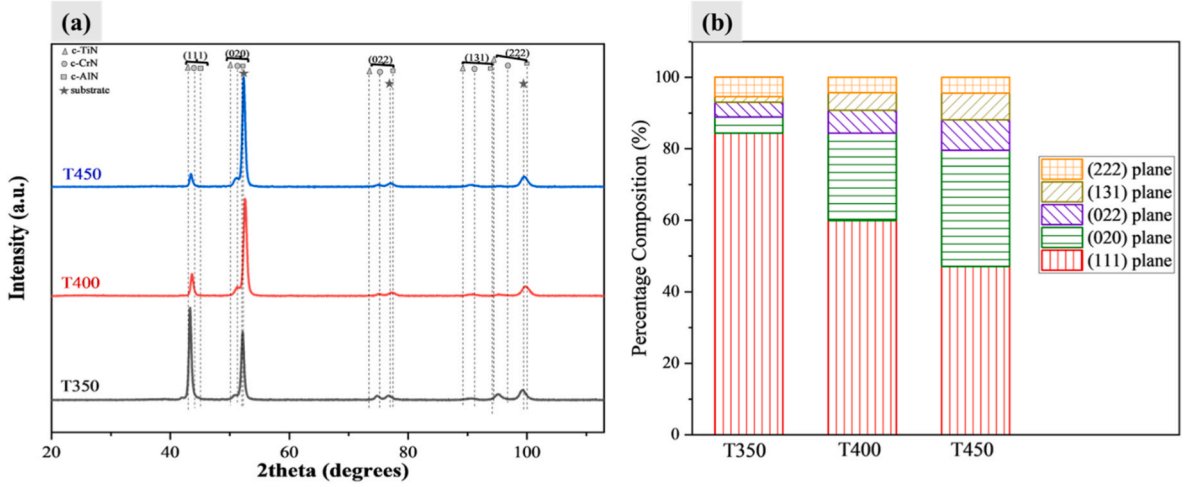

Fig. 7. (a) X-ray diffraction (XRD) patterns of AlTiN/AlTiCrN coatings deposited at different temperatures and (b) Relative crystallographic plane distribution of the coatings as a function of deposition temperature. *Note:* The percentage plane distribution was determined by normalizing the intensity of each diffraction peak to the total integrated intensity of all coating-related diffraction peaks [15].

deposition temperatures, as the X-rays more readily penetrate through the thinner coatings to the substrate [31]. This is corroborated by the cross-sectional micrographs (Fig. 6), where the coating thickness consistently reduced from T350 to T450. Meanwhile, the coating-related peaks were situated between the reference positions of c-TiN (96-101-1103), c-CrN (96-101-0975), and c-AlN (00-046-1200). However, the observed peak shifts towards either higher or lower 2θ angles relative to the reference peaks signify the formation of a substitutional solid solution of TiN, CrN, and AlN [3]. The typical resulting structure comprises coating atoms randomly occupying sites within the fcc NaCl-type lattice, causing lattice distortion, leading to the positioning of the peaks between referenced standards [18].

Furthermore, the coatings generally presented several crystallographic orientations, including (111), (020), (022), (131), and (222). It should be noted that some diffraction peaks, such as those observed near 51° and 91° indexed here as (020) and (131), may also be represented by equivalent indices such as (200) and (311), respectively. Explicitly, in previous reports on similar coating systems, these peaks are sometimes indexed as (200) and (311), which may stem from the use of alternative crystallographic reference databases, such as those provided by the

International Centre for Diffraction Data (ICDD/JCPDS) [27], whereas the present analysis employed the Crystallography Open Database. In addition, variations in the X-ray radiation source; Co Kα in the present study versus the more commonly used Cu Kα radiation, might also contribute to slight differences in peak positions and indexing conventions [32], [33]. Notably, at T350, the AlTiN/AlTiCrN coating exhibited an enhanced (111) preferential orientation. This is consistent with the findings from earlier studies, reporting a preferred (111) orientation for AlTiN/AlTiCrN coatings due to the high planar density of the closed-pack plane [3], [15]. However, as the deposition temperature increased to T450, (111) plane texturing diminished significantly, with its relative intensity decreasing from 84 to 47 % as shown in Fig. 7b. The reduction in the (111) texture with increasing deposition temperature could be attributed to the effect of energetic collisions and bombardment of the growing film by incoming species at elevated temperature. Such an occurrence disrupts the coating crystallinity and promotes competitive growth of other crystallographic planes [14], [15]. This results in the re-distribution of the coating atoms in more random plane orientations, evident in the general increase in (020), (022), (222), and (131) plane compositions (Fig. 7b), at higher temperatures. This observation is consistent with findings reported by Gui et al. [32], where energetic bombardment in sputtered AlTiCrN coatings promoted a shift in the preferred orientation from (111) to (200). Additionally, higher deposition temperatures enhance adatom mobility and facilitate defect annihilation, which promotes stress relaxation. This in turn reduces the driving force for (111) texture, thereby leading to a more random distribution of the crystallographic orientations [34], [35]. The reduction in the (111) plane orientation with increasing deposition temperature suggests a reduction in the densification of the coating structure, which has been associated with reduced tribological performance [3], [15].

Apart from the impact of the (111) plane on coating densification, it could also affect the roughness. In this regard, the emergence of more random plane orientations at elevated temperatures (Fig. 7b) may contribute to increasing surface roughness. This is based on the underlying principle that different planes exhibit varying growth rates; hence, the resulting competitive growth can lead to a less uniform surface morphology [2]. This might also explain why AlTiN/AlTiCrN coatings deposited at a lower temperature (T350), which contained fewer random planes, exhibited lower roughness values (Fig. 4). In summary, an increase in deposition temperature resulted in a reduction in the (111) plane texturing, accompanied by a competitive growth of other planes.

Further examination of the FWHM (full-width at half-maximum) values presented in Table 3 reveals the following distinct trends with increasing deposition temperature (T350 – T450): (1) peak broadening was observed for the (111) and (022) planes, as evidenced by the general increase in their FWHM values. (2) Peak narrowing was observed for the (020), (131), and (222) planes, indicated by the general reduction in their FWHM values.

These variations in the FWHM values suggest corresponding changes in the crystallite size and microstrain of the coatings. In general, higher FWHM values are associated with finer crystallite sizes and higher microstrain, whereas lower values typically signify coarser crystallites and reduced microstrain [3]. Using established equations from the literature [36], the average crystallite size and microstrain were calculated, with the results presented in Fig. 8.

The figure shows that increasing the deposition temperature (from T350 to T400) led to a general reduction in the average crystallite size from 11.6 to 10.4 nm, corresponding to an approximate 10.3 % reduction. However, a further increase in temperature in T450 resulted in an increase in the average crystallite size to 11.9 nm, representing a 14.4 % rise relative to T400. Comparable crystallite sizes, ranging between 9.9 and 13.2 nm, have been reported for AlTiN/AlTiCrN coatings with different layered architectures [3]. Ling et al. [8] previously reported a reduction in average crystallite size from 120 to 20 nm for AlCrN coatings with increasing deposition temperature from 250 to 450 °C, attributed to the increased impingement rate by the incoming adatoms, inhibiting crystallite growth. Their interpretation is consistent with the observations of this present study, with increasing deposition temperature from T350 to T400. Explicitly, the reduction in the average crystallite size (from T350 to T400) could be attributed to the enhanced coating bombardment by energetic species. This bombardment increases the impingement rate of the coating film, which suppresses the migration of crystallite boundaries, thereby leading to finer crystallites. In contrast, the subsequent increment in the average crystallite size from T400 to T450 is in agreement with previous findings by Warcholinski et al. [10], who observed 15 % increase in crystallite size of AlCrN coatings with increasing temperature from 350 to 450 °C. This occurrence could be attributed to the combined effect of higher deposition temperature, coupled with the additional heating resulting from increased energetic coating bombardment. These conditions promote adatom mobility and migration of crystallite boundaries, leading to crystallite coarsening [9], [10]. Nonetheless, compared to previous studies [8], [10], this study identifies critical temperature ranges where competing mechanisms (crystallite refinement versus coarsening) dominate, providing more insight into the temperature-dependent crystallite evolution in AlTiN/AlTiCrN coatings.

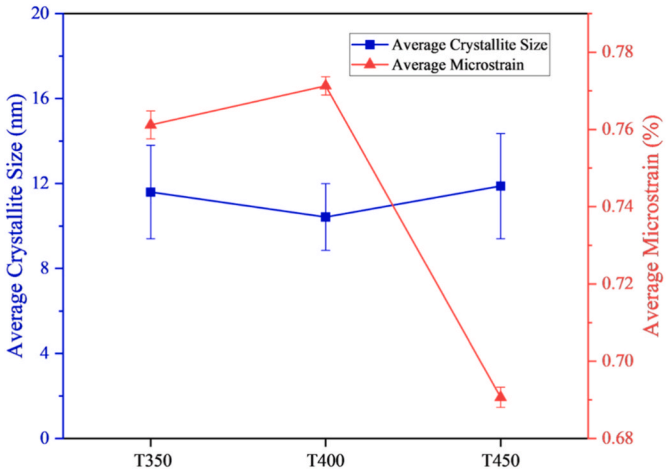

Fig. 8. Average crystallite size and microstrain for AlTiN/AlTiCrN coatings with different substrate roughness.

Furthermore, the figure reveals a slight increment in the average microstrain from 0.76 at T350 to 0.77 % at T400, followed by a dramatic decrease to 0.69 % at T450. Previous studies have reported microstrain values between 0.75 and 1.0 % for AlTiN/AlTiCrN coatings deposited on different substrate profiles [3], [15]. Generally, the occurrence of microstrain is attributed to defects such as vacancies, dislocations, and

Table 3
Peak positions and corresponding FWHM values of AlTiCrN/AlTiN coatings deposited at different temperatures.

Condition	(111) plane		(020) plane		(022) plane		(131) plane)		(222) plane	
	2θ (°)	FWHM (°)	2θ (°)	FWHM (°)	2θ (°)	FWHM (°)	2θ (°)	FWHM (°)	2θ (°)	FWHM (°)
T350	43.32	0.51	50.76	1.55	74.74	0.82	90.63	2.00	95.11	1.22
T400	43.67	0.58	51.27	1.32	75.16	1.13	90.88	1.99	95.21	1.35
T450	43.49	0.57	51.10	1.26	75.10	0.85	90.62	1.78	95.42	1.06

lattice distortions resulting from solid solution formation [35]. The dislocation density expressed as the total length of dislocation lines per unit volume, was computed using Equation (4) as follows [37]:

$$\delta = \frac{1}{D^2} \quad \text{Equation 4}$$

where δ represents dislocation density and D denotes the crystallite size. The computed dislocation density also aligns with the trend of the microstrain (Fig. 8). Explicitly, the dislocation density increased from 7.4 to 9.2 × 10^{15} lines/m^2 (T350 to T400), consistent with the increase in microstrain, driven by more intense energetic bombardment, following the increase in temperature. Meanwhile, the drastic strain relaxation upon further increase in temperature to T450 could be attributed to the annihilation of defects, evident in the reduction in dislocation density (to 7.0 × 10^{15} lines/m^2). Additionally, the reduced contribution of the (111) plane at higher temperatures (Fig. 7b) may also diminish lattice distortions resulting from substitutional and interstitial defects [14], thereby lowering microstrain at T450. This interpretation is consistent with previous studies indicating that higher microstrain in PVD coatings could be attributed to enhanced crystallographic ordering in the dense planes (such as the (111) plane), which promotes lattice distortion [15], [32]. In summary, increasing the deposition temperature (T350 – T400) initially resulted in finer crystallites and higher microstrain attributed to intensified energetic bombardment, but further temperature rise (T400 – T450) promotes migration of crystallite boundaries and defects annihilation, producing lower microstrain and larger crystallites.

3.2. Mechanical properties

3.2.1. Effect of deposition temperature on hardness and hardness-elastic modulus ratios

Fig. 9a presents the force-displacement curves obtained from the nanoindentation test, showing the loading and unloading stages. The positioning of the curves appears not to follow a distinct trend with deposition temperature. For instance, the T400 curve is positioned furthest to the left, while the T450 appears on the far right, with the T350 curve between them. The rightward shift of the curve results from deeper indenter penetration into the coating, suggesting greater coating deformation for T350 and T450, compared to T400. The deformation energy, calculated as the integral of the area under the force-displacement curve [35], supports this observation. Explicitly, the T400 exhibited the lowest deformation energy (3.28 nJ), with the highest recorded for T450 (3.97 nJ). The lower deformation energy at T400 implies reduced work by the indenter, owing to greater coating resistance. In line with established understanding, lower deformation energy and a leftward curve shift are indicators of higher coating hardness, evident in the T400 condition [3], [37]. Furthermore, the nanoindentation measurements were performed while ensuring that the maximum indentation depth was kept sufficiently small relative to the coating thickness to minimize substrate effects. Explicitly, across all deposition conditions, the maximum indentation depth, as indicated by the indenter displacement, was maintained within approximately 6 – 8 % of the total coating thickness, which is below the commonly accepted 10 % criterion for reducing substrate contribution to hardness measurements [38]. This indicates that the influence of the substrate's intrinsic hardness on the measured hardness values of the coatings is expected to be minimal, thereby supporting the reliability of the nanoindentation hardness results.

The hardness results presented in Fig. 9b further confirm that the T400 exhibited the highest hardness (36 GPa), reducing by about 13 % in T350 and 16 % in T450. These values are consistent with previous reports of AlTiN/AlTiCrN coatings, where hardness in the range of 27 – 34 GPa was observed under different substrate conditions and multilayer configurations [3], [32]. Additionally, the H/E and H^3/E^2 ratios are widely used indicators for evaluating the fracture resistance and tribological behaviour of PVD coatings, where higher values correlate with improved performance [2]. From Fig. 9b, the H/E ratio decreases slightly with temperature, from 0.072 at T350 to 0.068 at T450, corresponding to about 6 % reduction. Meanwhile, the H^3/E^2 ratio was lowest at T400 (0.177), with comparable values at T350 and T450 (~0.178). Given the error margins, these differences can be regarded as negligible [39]. Nonetheless, the ratios reported here align with those found in our previous study on AlTiN/AlTiCrN coatings deposited on different tool steels [15]. Overall, the higher H/E ratio at T350 indicates coatings deposited at T350 may offer superior fracture resistance [2]. Furthermore, concerns have been raised in prior studies that excessively high deposition temperatures can degrade the hardness of the tool steel substrate, thereby compromising cutting performance and tool life [40]. However, as shown in Table 4, the substrate hardness remained largely

Table 4
Hardness of tool steel substrates of AlTiCrN/AlTiN coatings deposited at different temperatures.

Condition	Hardness (GPa)
T350	5.97 ± 0.12
T400	6.00 ± 0.09
T450	5.94 ± 0.16

The tool steel substrate hardness was obtained using HV (GPa) = 0.00185 (P/d^2); P-load (N) and d-average diagonal length (mm) [42].

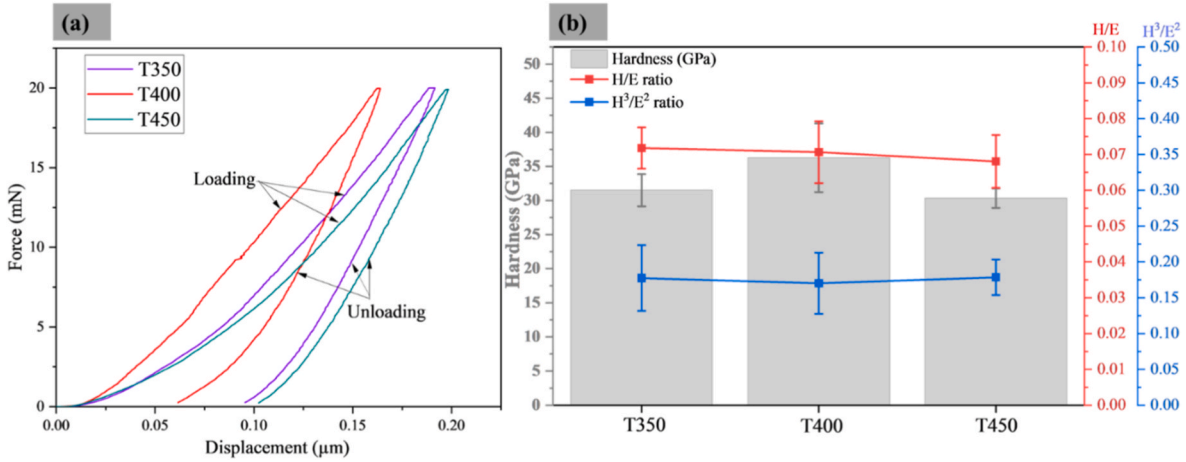

Fig. 9. (a) Load-displacement curves and (b) Hardness and indices of fracture resistance of the AlTiN/AlTiCrN coatings deposited at different temperatures.

unaffected by the deposition temperature, with values consistently around 6 GPa. The observed stability in substrate hardness could be attributed to the relatively low deposition temperatures employed (350 – 450 °C), which are below the critical tempering temperature of the A8 tool steel (~520 °C), and therefore likely unable to activate microstructural softening mechanisms such as carbide coarsening or martensite decomposition within the substrate matrix [41]. Consequently, the hardness of the substrate remained constant across the investigated deposition temperatures. In summary, while the coatings achieved the maximum hardness at T450, a balance of hardness with fracture resistance-related indices was obtained at T350.

3.2.1.1. Effect of (111) plane, crystallite size, and microstrain on hardness and fracture resistance. The hardness trend exhibited by the coatings could be explained in terms of factors such as the crystallographic orientation, crystallite size, and microstrain [3]. Fig. 10 shows the relationship between hardness and the (111) crystallographic plane. Previous studies have observed higher fractions of the densely packed (111) plane to enhance coating hardness through solid solution strengthening and impeding dislocation movement [18]. From the figure, no clear linear correlation between hardness and the (111) plane is observed in this study. For instance, the T350 condition, which contained the highest fraction of the (111) plane, presented a 13 % lower hardness than that of T400, despite having 24 % higher fraction of the (111) plane. This suggests that additional factors had a more dominant effect on the hardness of the coatings.

A clearer relationship is observed between crystallite size and hardness. Fig. 10 shows that an increase of about 14 % in crystallite size (from T400 to T450) corresponded to approximately 16 % reduction in the hardness. This behaviour aligns with the Hall-Petch phenomenon, where finer crystallites, as in the T400 condition, provide more boundaries that act as barriers to dislocation movement, thereby enhancing resistance to plastic deformation [43]. In support of this, Muhammed et al. reported a ~64 % increase in hardness in AlTiN/AlTiCrN-based layered coatings, associated with about 25 % reduction in crystallite size. The more pronounced effect observed in their study was attributed not only to fine crystallite size, but also to strengthening from multiple interfaces of the layered structure, as well as coating densification and strain hardening due to increased substrate bias [3].

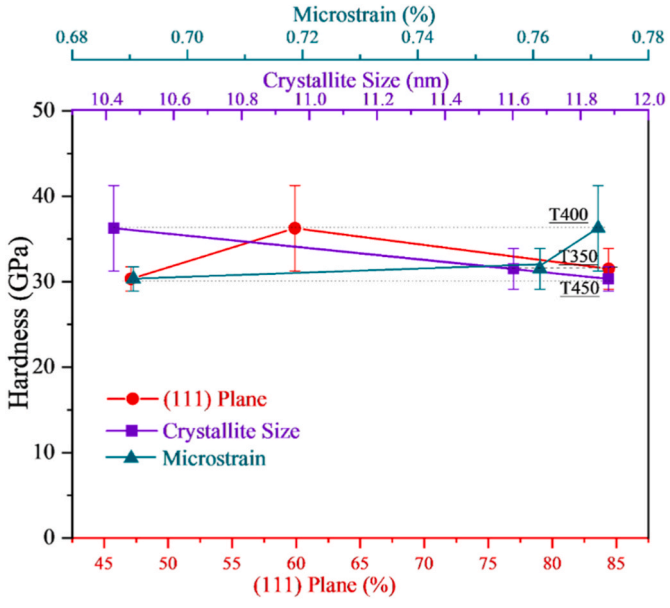

Fig. 10. Relationship between hardness, (111) plane orientation, crystallite size, and microstrain of AlTiN/AlTiCrN coatings at different deposition temperatures.

Furthermore, coating hardness could also be impacted by the microstrain. In this regard, increased microstrain introduces stress fields caused by lattice distortions during solid solution formation, which further hinders dislocation movement [44]. This effect is evident in the higher hardness of the T400, which exhibited about 11 % greater microstrain compared to T450. Further quantitative analysis revealed that a 1 % increase in microstrain and a 1 % decrease in crystallite size resulted in about 1.7 and 1.4 % increase in hardness, respectively. These results highlight that the microstrain exerted a stronger influence on hardness than the crystallite size. Additionally, the generally superior fracture resistance observed for T350, particularly in relation to T400, could be linked to its higher fraction of the densely packed (111) plane, which is effective at impeding crack initiation and propagation [15]. In summary, the enhanced hardness at T400 could be attributed to the dominant effect of higher microstrain and finer crystallites, while the superior fracture resistance at T350 is associated with its higher (111) plane fraction.

3.2.2. Effect of deposition temperature on adhesion strength

The scratch test results presented in Fig. 11a–c shows the variation of frictional force, normal load, and acoustic emissions with the scratch length at different deposition temperatures. The acoustic emissions, which represent signals generated by the indenter-coating interaction, were minimal within the first 1.2 mm of the scratch length for the T350 compared to the other coatings. Explicitly, the peak acoustic emissions in the first 1.2 mm reached approximately 6.5, 9.2, and 11.6 % for T350, T400, and T450, respectively. The increase in both the maximum peak intensity and their earlier occurrence with increasing deposition temperature indicates more severe coating failure and shorter time to failure [45]. Furthermore, fluctuations in the frictional forces were also observed at different deposition temperatures, particularly for T350, suggesting a higher coefficient of friction (COF) [46]. Fig. 11d illustrates the variation of the coefficient of friction (COF) with scratch length at different deposition temperatures. A general increase in COF is observed as the scratch length progresses, which may be attributed to the progressive increase in surface roughness and accumulation of debris during testing, consistent with a previous report by Zhang et al. [47]. Moreover, the COF evolution correlates well with the frictional force responses shown in Fig. 11a–c. In particular, the T350 condition, which exhibited the most pronounced fluctuations in frictional force, also recorded the highest COF, reaching a maximum value of approximately 0.70. In comparison, the T400 and T450 samples exhibited slightly lower maximum COF values of about 0.65 and 0.66, respectively. The higher COF exhibited at T350 could be linked to the relatively larger MP sizes (Fig. 2f), which promote stronger asperity interactions [2].

Further quantification of the coating adhesion strength was performed using the critical load corresponding to adhesive coating failure [3], with results presented in Fig. 12. The maximum critical load (~11 N) was obtained at T350, while T400 and T450 exhibited ~ 17 and 29 % lower values, respectively. This trend suggests superior adhesion strength at lower deposition temperatures. This is in agreement with the findings of Warcholinski et al. [10], who reported about a 17 % decrease in the critical load of AlCrN coatings deposited on tool steels as deposition temperature increased from 350 to 450 °C.

The superior adhesion strength observed at T350 could be explained by the combined effects of fracture resistance and coating roughness. As shown in Fig. 12b, the critical load increases with the fracture resistance index (H/E ratio). Consequently, the enhanced fracture resistance of T350 coatings enables them to absorb more energy during tribological interactions without fracturing. This increases the coating resistance to crack propagation, thereby lowering the likelihood of delamination under external loading [3]. Additionally, the lower roughness at T350 (Fig. 4a) further contributes to the enhanced adhesion strength. This is consistent with previous reports on AlTiN/AlTiCrN coatings, where smoother surface morphology was associated with enhanced adhesion

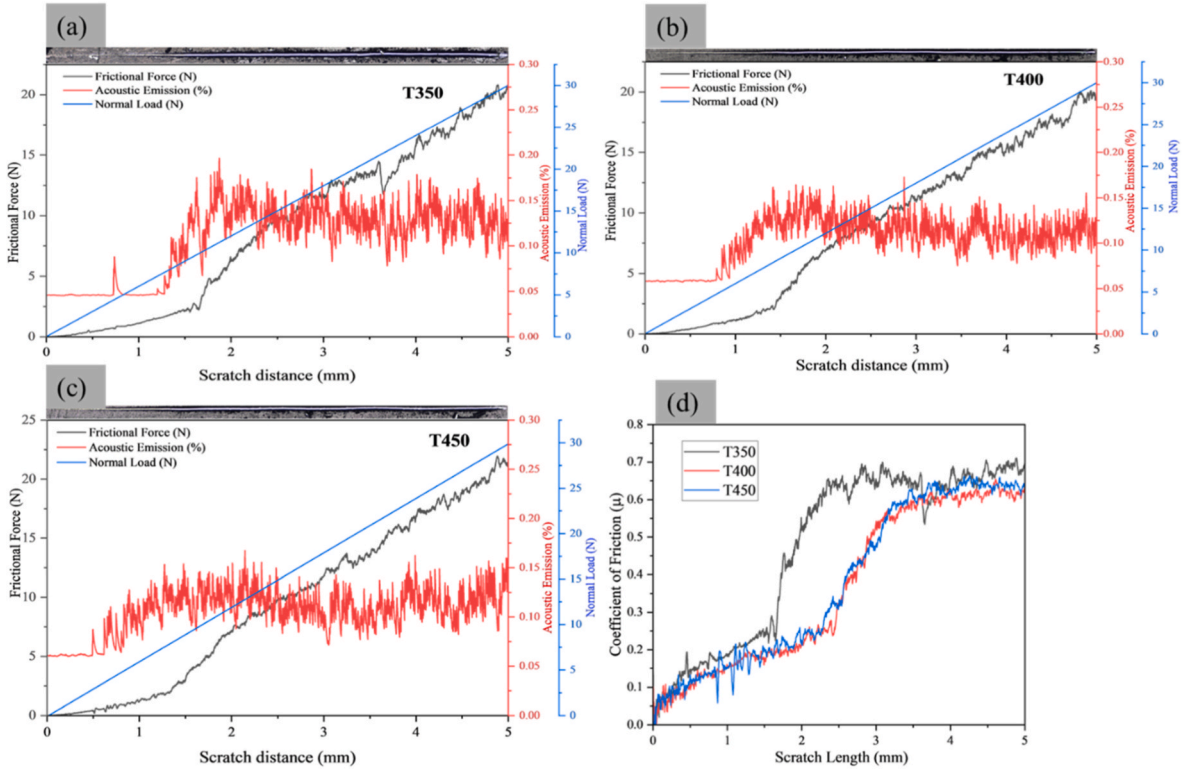

Fig. 11. Frictional force, acoustic emission, and normal load as a function of scratch length for AlTiN/AlTiCrN coatings: (a) T350; (b) T400; (c) T450; and (d) coefficient of friction at different temperatures.

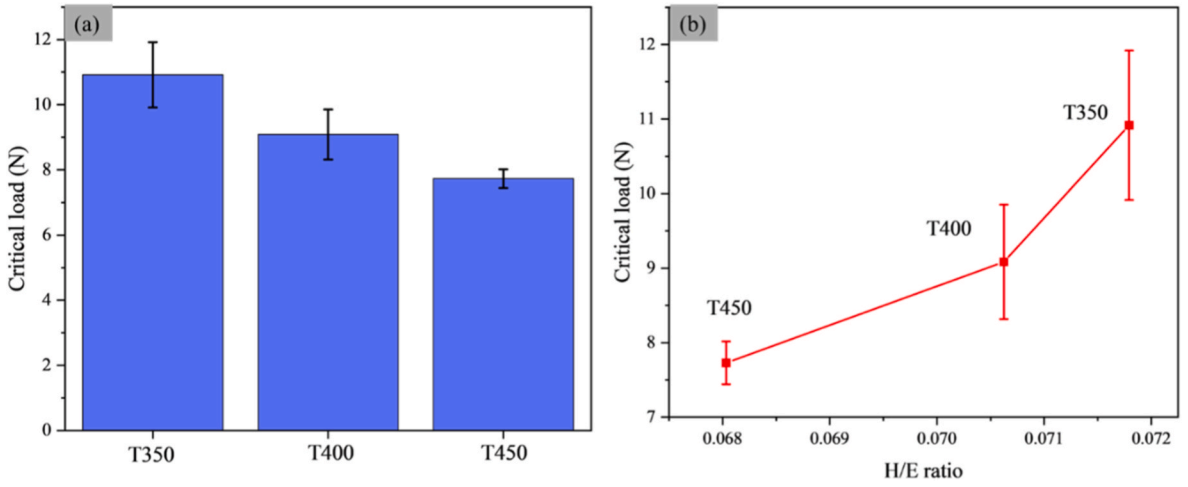

Fig. 12. (a) Critical load and (b) Relationship between critical load and H/E ratio for AlTiN/AlTiCrN coatings deposited at different temperatures.

strength [15]. This occurrence is attributed to the reduction of roughness-induced asperities that generate localized stresses leading to premature failure. Explicitly, a reduced surface roughness, as in the case of the T350 condition, minimizes the severity of surface asperities at the coating-abrasive interface, which are known to act as preferential sites for stress concentration during tribological interactions. Consequently, the minimal occurrence of such asperities could suppress generation of localized stresses, thereby reducing the likelihood of crack initiation and subsequent coating delamination [22]. In summary, superior adhesion strength obtained at lower deposition temperature could be attributed to lower roughness and enhanced fracture toughness.

3.3. Wear resistance

Fig. 13 shows the wear rates of the coatings, with the T350 condition exhibiting the least wear rate (~2×10^{-4} mm^3/Nm), suggesting superior wear resistance at lower deposition temperature. With increasing deposition temperature, the wear rate increased by about 36 and 52 % at T400 and T450, respectively. These wear rate values are comparable to those previously reported for cathodic arc evaporated AlTiN/AlTiCrN coatings, which were in the range of 1.8 – 2.2 $\times 10^{-4}$ mm^3/Nm [15].

Further analysis of the wear track of the samples was conducted to gain insights into the wear mechanisms. The results of the analysis presented in Fig. 14 reveal the presence of two distinct zones. The dark zone (Zone A; Fig. 14a–c) contained predominantly coating elements

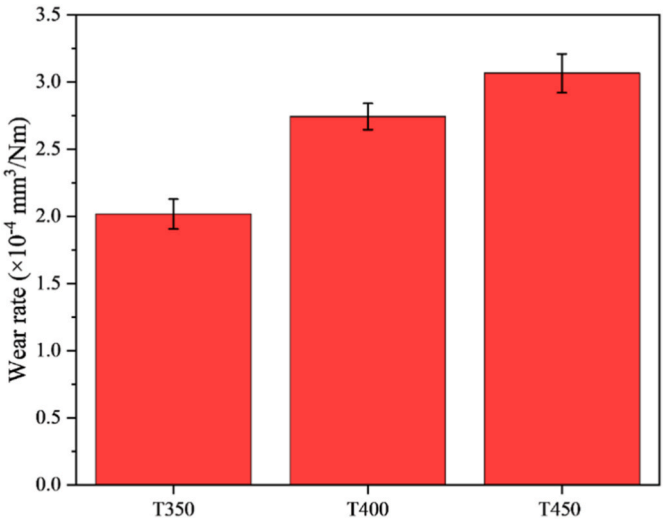

Fig. 13. Wear rates of the AlTiN/AlTiCrN coatings at different deposition temperatures.

(such as Al, Ti, and N) with relatively low Fe content, as confirmed by EDX analysis (P1-3, Table 5). This indicates the retention of coating material in these regions. Meanwhile, the bright zone (Zone B; Fig. 16d–f) presented higher Fe content alongside reduced coating elements (P4-6, Table 5), signifying complete coating removal leading to substrate exposure [3]. Further examination of the exposed substrate region (zone B) revealed the occurrence of abrasive microcutting grooves at all deposition temperatures. This is likely due to the higher hardness of the abrasive silica particle (about 8.5 GPa [48]), compared to the tool steel substrate (about 6 GPa, Table), which provides the driving force for abrasive wear, in the form of microcutting grooves [49]. To further elucidate the wear mechanisms, cross-sectional micrographs of the wear tracks were obtained (Fig. 14g–i). The cross-section corresponding to the T350 condition (Fig. 14g) reveals a relatively narrower wear track (~14,417 μm) and shallower penetration into the substrate, with a wear depth of approximately ~312 μm. In comparison, the T400 and T450 conditions (Fig. 14h and i) exhibit wider and deeper wear tracks, indicating a greater extent of material removal. Specifically, the wear track width increased by about 2.4 % and 3.9 %, respectively, while the wear depth increased by approximately 10.6 % and 16.0 % relative to the T350 condition. These observations indicate that the T350 coating provides improved resistance to abrasive wear.

Table 5
EDX analysis of the worn samples (corresponding to Fig. 14).

Spectra	Composition (at. %)						
	Al	Ti	Cr	N	O	Si	Fe
P1	23.0	14.9	0.6	46.9	9.0	0.3	5.3
P2	20.8	15.4	1.7	34.6	19.0	1.0	7.6
P3	19.7	15.2	6.6	45.2	11.7	0.1	1.6
P4	4.6	1.9	7.6	1.0	11.5	2.8	70.5
P5	0.2	0.3	6.6	–	27.5	7.4	58.1
P6	0.3	0.1	9.4	–	3.4	2.5	84.3

Note: Given the qualitative nature of EDX analysis, the results presented in this table are intended solely for comparative evaluation across the investigated deposition temperatures.

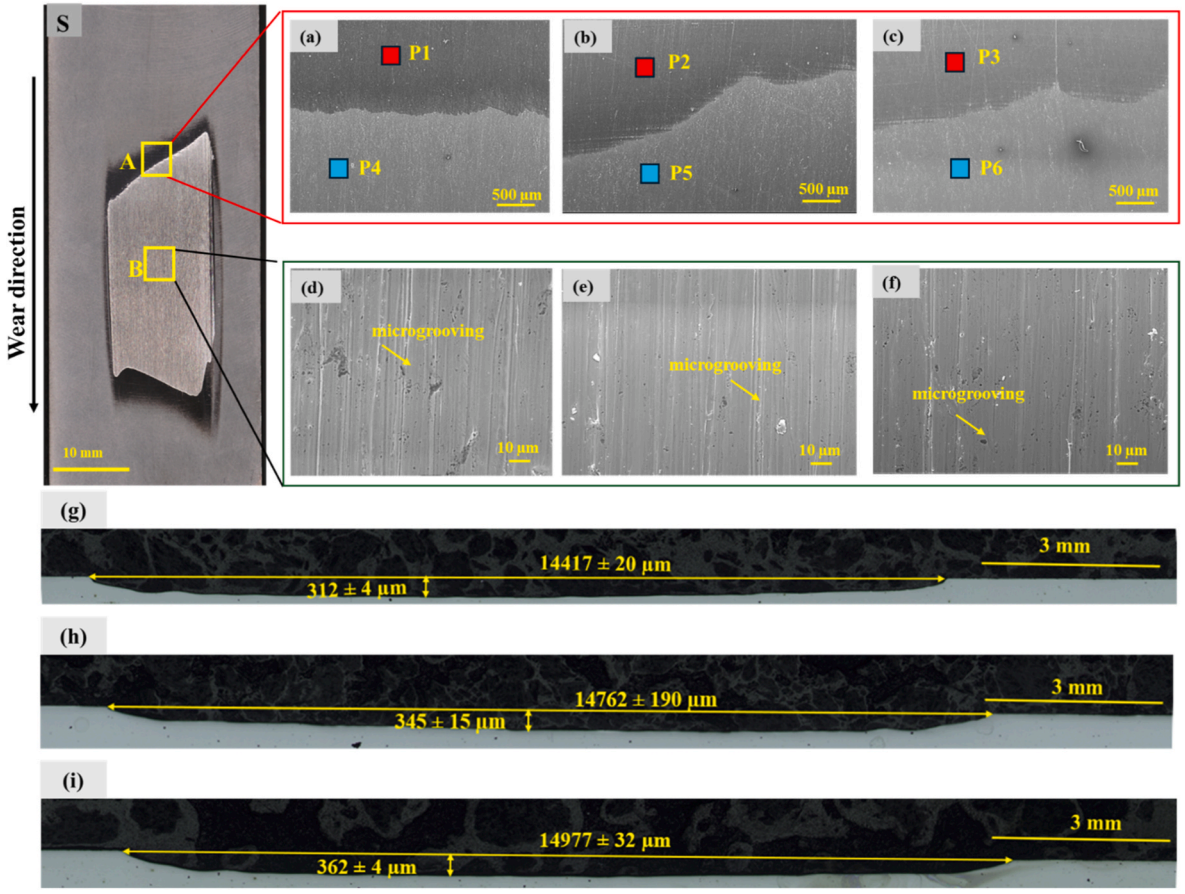

Fig. 14. Micrographs of the wear tracks for the investigated coatings: (S) overview of the wear track; (a, d) T350; (b, e) T400; (c, f) T450. Cross-sectional micrographs of the wear tracks: (g) T350; (h) T400; (i) T450.

Consequently, the smaller wear track dimensions observed for the T350 condition are consistent with the lower wear rates reported in Fig. 13.

In addition, silica contamination (third-body in the wear test), known to facilitate tribochemical coating degradation [2], was also detected in both coating-containing and substrate-exposed regions. Notably, the relatively higher levels of Si contamination recorded in the region of the exposed substrate (2.5 – 7.5 wt %, P4-6, Table 5) compared to the coating-containing region (0.3 – 1.0 wt %, P1-3, Table 5) highlight the protective role provided by the AlTiN/AlTiCrN coating in limiting silica-induced damage. Explicitly, the hard silica particles trapped at the sliding interface can cause micro-cutting and localized stress, stripping away protective coating layers and exposing fresh material to further mechanical attack [50], [51]. In this study, the AlTiN/AlTiCrN coating acted as a protective barrier by preventing silica particles from embedding and safeguarding the underlying substrate in the coating-containing regions. More so, the presence of O detected in the wear track is most likely due to atmospheric exposure during wear testing, consistent with previous reports [52]. In summary, increasing the deposition temperature led to reduced wear resistance, as evidenced by the higher wear rates. The wear tracks for all temperature conditions (T350 – T450) exhibited a consistent wear behaviour pattern, characterized by regions of partially abraded coating alongside exposed substrate with prominent micro-cutting grooves. This reflects a dominant three-body abrasive wear mechanism that remains fundamentally unchanged across the studied temperature range. The degradation primarily involves a transition from protective coating-dominated abrasion to substrate-driven abrasive wear.

3.4. Corrosion properties

Fig. 15a presents the EIS spectra of the AlTiN/AlTiCrN coatings deposited at different temperatures. In this figure, the size of the imperfect semicircular arc, which represents the capacitive response of the coating, reflects its corrosion resistance. Generally, larger arcs correspond to better corrosion resistance [18], [53]. From the figure, the T350 and T450 coatings exhibited the largest capacitive arc, signifying the superior electrochemical stability and corrosion resistance. Meanwhile, the T400 condition displayed noticeably smaller arc, implying a comparatively lower electrochemical performance at intermediate deposition temperature. In contrast, the uncoated substrate exhibited the smallest capacitive arc, indicating significantly lower corrosion resistance compared with the coated samples. This behaviour highlights the protective role of the AlTiN/AlTiCrN coatings in enhancing the electrochemical stability of the substrate by acting as an effective barrier against electrolyte penetration. Overall, the EIS results demonstrate that coatings deposited at T350 and T450 provide the most stable electrochemical response and superior corrosion resistance among the investigated conditions.

To further quantify the influence of deposition temperature on the coatings' corrosion behaviour, PDP measurements were performed. Fig. 15b shows the PDP curves (or Tafel plots) of the AlTiN/AlTiCrN coatings deposited under different temperature conditions. The plots revealed a systematic shift of the corrosion potential (E_{corr}) toward a more negative value, with increasing deposition temperature from T350 to T450, evident by the downward shift of the Tafel curves. This is also reflected by the decrease in the E_{corr} from – 427 to 469 mV with increasing deposition temperature, as shown in Table 6. This is consistent with prior reports linking more positive potentials, such as those at lower deposition temperature, to improved corrosion performance [54]. The figure also includes the response of the uncoated substrate, allowing a direct comparison between the coated and uncoated conditions. Overall, the coated samples exhibit a clear modification of the polarization behaviour compared with the substrate, indicating that the presence of the coating alters the electrochemical response of the surface. In particular, the T350 coating shows a noticeable shift of the E_{corr} toward a more positive value relative to the substrate, suggesting a reduced thermodynamic tendency for corrosion.

Furthermore, complementary metrics such as i_{corr} and R_p obtained via the Tafel extrapolation method [21], presented in Table 6, were also evaluated to gain additional insights. Generally, lower i_{corr} and higher R_p values correspond to reduced corrosion activity, translating to enhanced corrosion protection [55]. Compared with the substrate, which exhibits a relatively high i_{corr} (26.5 μA/cm^2) and a low R_p (1.1 kΩ cm^2), all coated samples demonstrate substantially lower corrosion current densities and higher polarization resistance values. This clearly indicates that the AlTiN/AlTiCrN coatings act as an effective barrier that limits electrolyte interaction with the underlying substrate and significantly improves corrosion resistance. From the table, T400 coating exhibited the highest i_{corr} (14.7 μA/cm^2) and the lowest R_p (1.2 kΩ cm^2), suggesting its inferior corrosion resistance. Meanwhile, the T350 and T450 coatings generally displayed lower i_{corr} (<14.1 μA/cm^2) and higher R_p (>1.5 kΩ cm$^{2)}$ values, indicative of superior corrosion performance. It is worth noting that although the T450 (– 469 mV) coating exhibits a slightly more negative E_{corr} compared with T400 (– 464 mV), it displays a lower i_{corr}. This behaviour can be explained by the fact that E_{corr} primarily reflects the thermodynamic tendency of a material to corrode, whereas i_{corr} is directly related to the kinetics of the corrosion reactions. Consequently, a more negative E_{corr} does not necessarily imply a higher corrosion rate if the electrochemical reactions at the surface are kinetically suppressed [56], [57]. In the present case, the lower i_{corr} observed for the T450 coating suggests that the electrochemical reactions occurring at the coating/electrolyte interface are

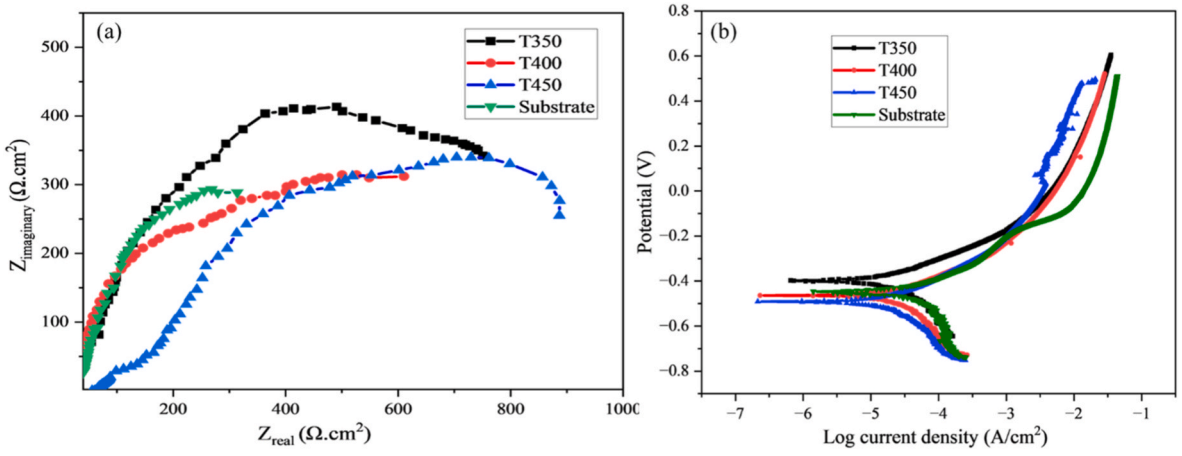

Fig. 15. (a) Electrochemical impedance spectroscopy (EIS) spectra of AlTiN/AlTiCrN coatings deposited at different temperatures and (b) Potentiodynamic polarization (Tafel) curves of the coatings as a function of deposition temperature.

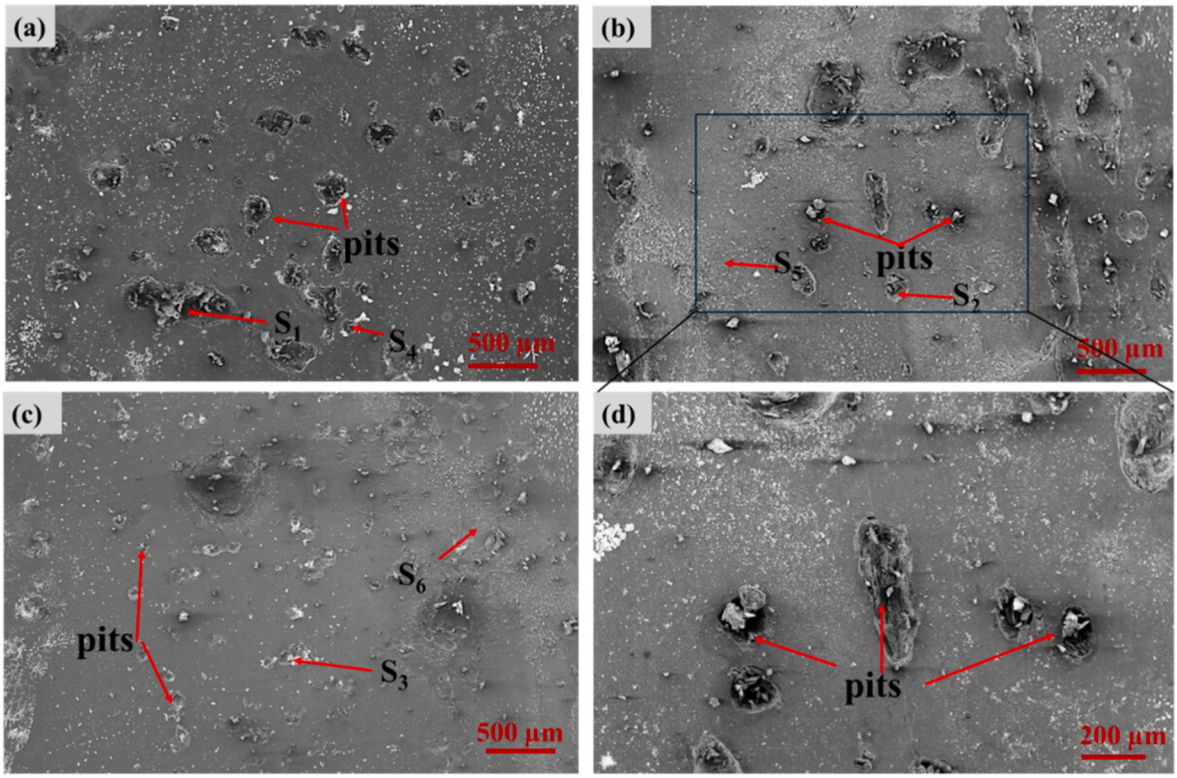

Fig. 16. Micrographs showing the corroded surface morphology of AlTiN/AlTiCrN coatings deposited at different temperatures: (a) T350, (b) T400, and (c) T450; (d) Higher-magnification image at T400, highlighting some corrosion pits located beneath some macroparticles.

Table 6
Potentiodynamic polarization parameters, coating porosity, and protective efficiency of AlTiN/AlTiCrN coatings prepared at different deposition temperatures.

Condition	E_{corr} (mV)	i_{corr} (µA/cm^2)	βa (mV)	βc (mV)	R_p (kΩ.cm^2)	Porosity (%)	Protective efficiency (%)
Substrate	−466.2 ± 13.8	26.5 ± 2.1	117.1 ± 4.8	−134.1 ± 19.8	1.1 ± 0.2	–	–
T350	−427.3 ± 28	12 ± 2.0	103.1 ± 8.1	−145.1 ± 5.9	2.2 ± 0.6	0.52 ± 0.1	54.9 ± 6.3
T400	−463.9 ± 4.0	14.7 ± 2.0	104.2 ± 6.0	−161.5 ± 8.0	1.2 ± 0.2	0.93 ± 0.1	44.6 ± 7.6
T450	−468.9 ± 19.4	14.0 ± 0.8	100.4 ± 17.1	−156.4 ± 27.6	1.6 ± 0.3	0.67 ± 0.1	47.0 ± 2.9

more effectively hindered compared with the T400 coating. Similar behaviour has been reported in previous studies where lower i_{corr} values were observed despite shifts of E_{corr} toward more negative potentials, indicating that corrosion resistance is more strongly governed by kinetic factors represented by i_{corr} rather than E_{corr} alone [58]. Additionally, the porosity of the coatings followed a similar trend, with the T350 and T450 showing the lowest porosity (<0.7 %), while T400 showed the highest porosity (~0.9 %), which promotes electrolyte penetration and accelerates coating degradation [59]. Consequently, the protective efficiency was lowest for T400 (~44 %) compared to over 50 % for T350 and 47% for T450 (Table 6). These results further highlight the beneficial role of the coating in mitigating corrosion compared with the bare substrate, while also demonstrating that the effectiveness of the protective barrier is strongly influenced by the deposition temperature.

Further examination of the surface of the corroded samples is presented in Fig. 16. The figure revealed the occurrence of pitting corrosion characterized predominantly by circular pits across all conditions. Similar occurrences of pitting corrosion have been reported for AlTiN/AlTiCrN coatings deposited on different substrate finishes [3]. The pits appear to be prominent in the T400 condition (Fig. 16b), suggesting severe coating degradation. Further EDX analysis of the corroded surface presented in Table 7 revealed the presence of coating elements (Al, Ti, Cr, N) alongside O and electrolyte components (Na and Cl). The relatively higher O levels observed in spectra S_1, S_5, and S_6 alongside metallic coating components (Al, Ti, and Cr) indicate possible formation of passive oxide layers [54]. Further evaluation revealed that the localized pitting could result in substrate exposure, reflected in relatively higher Fe content, particularly in Spectra S_2 and S_3. In summary, the EIS and PDP analyses revealed that coatings deposited at T350 and T450 demonstrated superior electrochemical stability and lower porosity, resulting in enhanced corrosion protection.

Table 7
EDX elemental analysis of the corroded AlTiN/AlTiCrN coatings shown in Fig. 16.

Spectra	Elemental composition (at. %)							
	Al	Ti	Cr	N	O	Na	Cl	Fe
S_1	11.5	9.2	17.8	–	58.8	2.4	0.3	–
S_2	2.8	1.3	16.6	–	26.9	–	1.5	51.0
S_3	0.5	0.4	7.4	–	18.4	2.0	8.9	62.6
S_4	9.9	8.8	16.0	–	1.9	41.9	21.6	–
S_5	8.2	5.6	9.6	–	65.5	1.6	0.5	9.0
S_6	9.2	8.0	11.5	5.7	59.5	1.2	0.2	4.8

4. Discussion

The variations in the wear and corrosion behaviour of the AlTiN/AlTiCrN coatings with deposition temperatures could be explained by the differences in their morphological and microstructural

characteristics such as MP statistics (Fig. 2f), coating thickness (Fig. 5), coating composition (Fig. 7, Table 2), microstrain and crystallite size (Fig. 8), as well as their mechanical properties including hardness and H/E ratio (Fig. 9), and adhesion strength (Fig. 12). These discussions are elaborated under the following subsections.

4.1. Influence of coating properties on wear performance

The relationship between the wear rate, hardness, and H/E ratio of the AlTiN/AlTiCrN coatings deposited at different temperatures is presented in Fig. 17a. Previous studies have reported that coatings with reduced hardness typically exhibit higher wear rates [3], [18]. In the present study, although no clear linear correlation was observed between the wear rates and the hardness, the relatively lower hardness of the T450 coating might have contributed to its higher wear rates. In this regard, the lower hardness diminishes the load-bearing capacity of the coating and resistance to plastic deformation, culminating in more material removal, leading to higher wear rates [35]. Meanwhile, the T350 coating demonstrated superior wear resistance despite having a lower hardness compared to the T400, suggesting the influence of additional factors.

Furthermore, as shown in Fig. 17a, the H/E ratio exhibited an inverse relationship with wear rates, with higher values corresponding to lower wear rates, as observed in the T350 coating. The current finding corroborates previous research, which established that PVD coatings with greater H/E ratios tend to exhibit better wear performance [18], [28]. Consequently, the superior wear resistance of the T350 coating could be attributed to its higher H/E ratio, which enhances the coating's elastic strain tolerance and fracture toughness. This improvement helps to resist crack initiation and propagation during abrasive loading, thereby reducing material loss [60]. Further quantitative analysis to ascertain the sensitivity of the wear rates to changes in hardness and H/E ratio revealed that 1 % decrease in hardness and H/E ratio from T350 to T450 resulted in about 14.0 and 9.9 % increments in the wear rates, respectively, suggesting that the hardness exerts a greater influence on the wear behaviour compared to the H/E ratio.

The relationship between the adhesion strength (i.e., critical load), coating thickness, and surface roughness is presented in Fig. 17b. From the figure, a negative correlation is observed between wear rates and both critical load and coating thickness, where higher critical loads and thicker coatings are associated with lower wear rates (i.e., T350). This is consistent with findings from our previous study, where we observed AlTiN/AlTiCrN-based coating architectures with higher coating thickness and critical load consistently exhibited superior wear performance [3]. The 52 % lower wear rates observed at higher critical load in T350 coating could be attributed to stronger interfacial bonding, evident in the 17 % higher critical load relative to T450, which minimizes the risk of coating delamination during abrasive contact [60]. In addition, the thicker T350 coatings offer improved load-bearing capacity, which reduces shear stress by distributing the applied load over a larger material volume, thereby mitigating material removal compared to the thinner T400 and T450 coatings [15].

Furthermore, despite no distinct linear relationship being observed between the surface roughness and wear rate, coatings with higher surface roughness (such as in the T400 and T450) exhibited higher wear rates. This is consistent with findings from previous studies [3], which associated increased surface roughness with more pronounced surface asperities that act as initiation sites for localized stress accumulation. Consequently, the T350 coating's smoother surface, on the other hand, minimizes stress concentration, leading to reduced material loss; hence, the lower wear rates [2]. Further quantitative analysis revealed that a 1 % decrease in critical load and coating thickness, and a 1 % increase in average roughness from T350 to T450, resulted in 1.8, 3.6, and 5.6 % increments in the wear rate, indicating that the surface roughness has the most significant impact on the wear rates among the parameters. In summary, the wear rates decreased with the H/E ratio, coating thickness, and adhesion strength, translating to improved tribological behaviour at higher values of these parameters, as in the T350 condition. Conversely, coatings with higher roughness (T400 and T450) displayed elevated wear rates, indicating poorer performance. The quantitative analysis revealed that the impact of the properties on the wear performance of the coatings ranks in the decreasing order: hardness > H/E ratio > roughness > coating thickness > adhesion strength. The superior wear resistance of the T350 coating can therefore be attributed to its intermediate hardness, higher H/E ratio, smoother surface, greater coating thickness, and stronger interfacial bond; all of which enhanced its load-bearing capacity and resistance to crack propagation under sliding conditions.

4.2. Influence of coating properties on corrosion resistance

The corrosion behaviour of the AlTiN/AlTiCrN coatings could be explained by the combined influence of their structural, compositional, and microstructural characteristics [3]. For instance, both the T350 and T450 coatings benefit from a denser coating structure; achieved in the case of T350 through a higher fraction of close-packed (111) planes (Fig. 7b), and in T450 through enhanced energetic bombardment during deposition. The coating densification is reflected in their relatively lower porosity (see Table 6), which limits electrolyte penetration into the coating microstructure, thereby reducing corrosion susceptibility [61].

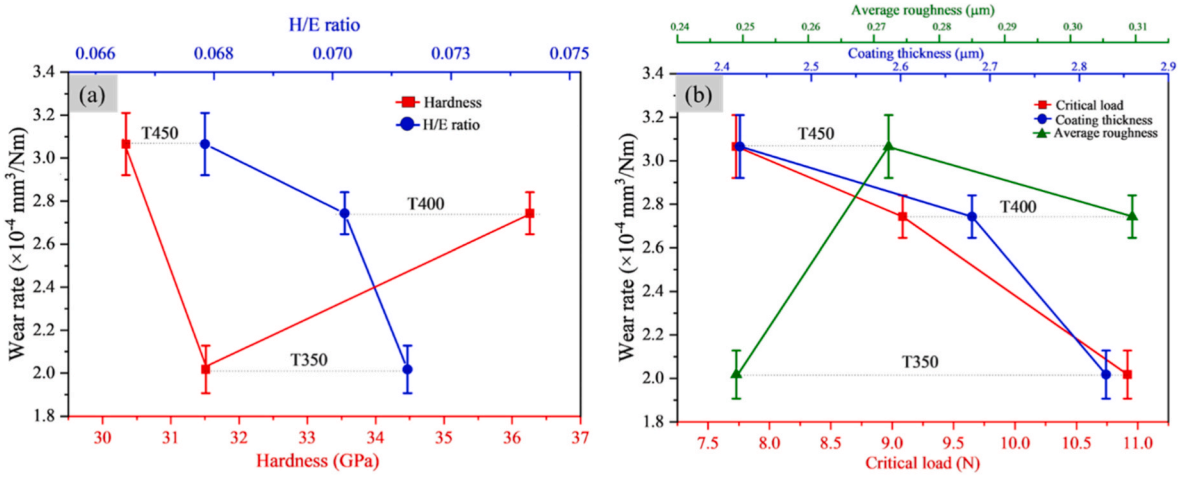

Fig. 17. (a) Correlation between wear rate, hardness, and H/E ratio of AlTiN/AlTiCrN coatings deposited at different temperatures, and (b) Correlation between wear rate, critical load, coating thickness, and surface roughness as a function of deposition temperature.

Similar observations have been reported for AlTiN/AlTiCrN multilayer coatings, where energetic adatom bombardment under higher biasing conditions led to a more compact structure with reduced porosity and improved corrosion resistance [3]. Additionally, the T350 and T450 also benefit from thick coatings (see Fig. 5) and coarser crystallites (See Fig. 8), which further contribute to their superior corrosion resistance. In this regard, a thicker coating, as seen particularly in the T350 (Fig. 5a), extends the diffusion path for the corrosive medium, delaying electrolyte access to the substrate and slowing the degradation process. Likewise, since crystallite boundaries often serve as initiation sites for electrochemical reactions, the coarser crystallite structure of T350 and T450 (Fig. 8) provides fewer active sites for corrosion initiation, leading to lower corrosion rates [35].

Furthermore, in addition to the finer coating crystallite, factors such as MP density and the Cr content of the top AlTiCrN layer could also contribute to the inferior corrosion protection offered by the T400 coating. For instance, the T400 coating exhibits a higher MP density, which serve as preferential sites for galvanic cell initiation and subsequent electrochemical degradation [62]. Higher-magnification analysis (Fig. 16d) reveals the occurrence of pitting localized beneath some MPs. These inherent defects act as physical discontinuities in the coating, creating pathways for electrolyte penetration and subsequent localized attack. Previous studies have shown that these MPs are typically metal-rich and nitrogen-deficient, especially when embedded within the coating matrix [2]. As a result, they are more susceptible to attack by the corrosive medium. The progressive dissolution of these MPs leads to the formation of surface craters, which in turn accelerate the overall degradation by exposing new surfaces to the electrolyte. This occurrence is less likely for the T350 and T450, due to their relatively lower MP density, hence their superior performance. Additionally, previous studies have also observed that, in layered coating architecture, the composition of the top layer is critical in the corrosion performance [3]. Consequently, the 13 % lower Cr content of the AlTiCrN top layer in the T400 coating (relative to T350, see Table 2) might further compromise its corrosion resistance. Chromium plays a vital role in forming stable passive films; thus, reduced Cr content weakens passivation and increases the likelihood of localized attack [54]. Overall, the superior corrosion performance exhibited by the T350 and T450 coatings could be attributed to the effect of dense coating structures, coating thickness, and coarser crystallites, which collectively reduce electrolyte penetration and transfer to the substrate, thereby minimizing corrosion attack. Meanwhile, the T400 coating exhibited inferior resistance, primarily due to its finer crystallite structure, higher MP density, and lower Cr content in the top layer; factors that promote localized corrosion and faster degradation.

5. Conclusion

The following are the key findings from the study on the effect of deposition temperature (350 – 450 °C; T350 – T450) on the wear and corrosion behaviour of AlTiN/AlTiCrN ceramic coatings deposited on AISI A8 tool steel:

1. The macroparticle (MP) characteristics varied with deposition temperature and influenced the surface roughness. Specifically, lower MP density at T350 resulted in a smoother surface, whereas the higher MP density at T400 led to increased surface roughness.
2. Increasing the deposition temperature reduced coating thickness and (111) plane texturing, while all coatings maintained stoichiometric compositions with nearly constant Al/(Al + Ti + Cr) ratio.
3. Maximum hardness occurred at T400, driven by finer crystallites and higher microstrain. However, T350 provided the optimal balance of hardness and fracture resistance, attributed to its higher (111) plane fraction. Additionally, the superior adhesion strength of T350 was attributed to its smoother surface and enhanced fracture resistance.
4. Wear performance was influenced by mechanical and microstructural factors, with T350 exhibiting superior wear performance. The wear rates decreased with increasing H/E ratio, coating thickness, and adhesion strength, but increased with roughness. Quantitative analysis ranked the influence of coating properties on wear as: hardness > H/E ratio > roughness > coating thickness > adhesion strength.
5. The T350 and T450 coatings demonstrated superior corrosion resistance due to their denser structure, coating thickness, and coarser crystallites, which restricted electrolyte penetration. The inferior T400 behaviour was linked to its finer crystallites, higher MP density, and lower Cr content in the top layer, promoting localized attack and faster degradation.

CRediT authorship contribution statement

Musa Muhammed: Writing – original draft, Methodology, Investigation, Formal analysis, Data curation, Conceptualization. **Mousa Javidani:** Writing – review & editing, Supervision, Resources, Project administration, Methodology, Funding acquisition, Formal analysis, Conceptualization. **Majid Heidari:** Writing – review & editing, Methodology, Investigation, Conceptualization. **Tom Levasseur:** Writing – review & editing, Methodology, Conceptualization. **Mohammad Jahazi:** Writing – review & editing, Project administration, Methodology, Investigation, Funding acquisition, Data curation, Conceptualization.

Funding

This study was supported by the Natural Sciences and Engineering Research Council of Canada (NSERC), and Consortium de Recherche et Innovation en Transformation Métallique (CRITM) under the Grant No. ALLRP 571323-21.

Declaration of competing interest

The authors declare that they have no known competing financial interests or personal relationships that could have appeared to influence the work reported in this paper.

Acknowledgments

The authors would like to acknowledge the financial support from the Natural Sciences and Engineering Research Council of Canada (NSERC), Consortium de Recherche et Innovation en Transformation Métallique (CRITM), and the industrial partners of the project DK-Spec, Québec, Canada, and Forezienne, France, under the Grant No. ALLRP 571323-21. The authors also acknowledge the contribution of Tahere Ebrahimi Sadrabadi for her assistance in conducting some of the experimental work.

References

[1] B. Warcholinski, A. Gilewicz, Surface engineering of woodworking tools, a review, Appl. Sci. 12 (20) (2022) 1–19, https://doi.org/10.3390/app122010389.
[2] M. Muhammed, M. Javidani, T. Ebrahimi Sadrabadi, M. Heidari, T. Levasseur, M. Jahazi, A comprehensive review of cathodic arc evaporation physical vapour deposition (CAE-PVD) coatings for enhanced tribological performance, Coatings 14 (3) (Feb. 2024) 246, https://doi.org/10.3390/coatings14030246.
[3] M. Muhammed, M. Javidani, T. Ebrahimi Sadrabadi, M. Heidari, T. Levasseur, M. Jahazi, Effect of layered architectural design on the tribological behaviour of AlTiN/AlTiCrN-based cathodic arc evaporated physical vapour deposition coatings, Metall. Mater. Trans. A 56 (7) (Jul. 2025) 2513–2536, https://doi.org/10.1007/s11661-025-07802-8.
[4] B. Warcholinski, A. Gilewicz, J. Ratajski, Z. Kuklinski, J. Rochowicz, An analysis of macroparticle-related defects on CrCN and CrN coatings in dependence of the substrate bias voltage, Vacuum 86 (9) (Mar. 2012) 1235–1239, https://doi.org/10.1016/j.vacuum.2011.04.023.

[5] B. Warcholinski, A. Gilewicz, The properties of multilayer CrCN/CrN coatings dependent on their architecture, Plasma Process. Polym. 8 (4) (Apr. 2011) 333–339, https://doi.org/10.1002/ppap.201000167.

[6] C. Wächtler, C. Wüstefeld, M. Šíma, J. Pikner, D. Rafaja, Influence of the substrate treatment on the microstructure and properties of chemical vapour deposited Ti(C, N) coatings, Surf. Coating. Technol. 466 (May) (2023), https://doi.org/10.1016/j.surfcoat.2023.129675.

[7] M. Ali, E. Hamzah, M.R. Toff, Friction coefficient and surface roughness of TiN-coated HSS deposited using cathodic arc evaporation PVD technique, Ind. Lubric. Tribol. 60 (3) (2008) 121–130, https://doi.org/10.1108/00368790810871048.

[8] C.L. Ling, et al., Effect of substrate roughness and PVD deposition temperatures on hardness and wear performance of AlCrN-coated WC-Co, Surf. Coating. Technol. 436 (January) (2022) 128304, https://doi.org/10.1016/j.surfcoat.2022.128304.

[9] C. Gautier, J. Machet, Study of the growth mechanisms of chromium nitride films deposited by vacuum ARC evaporation, Thin Solid Films 295 (1–2) (1997) 43–52, https://doi.org/10.1016/S0040-6090(96)09164-X.

[10] B. Warcholinski, A. Gilewicz, P. Myslinski, E. Dobruchowska, D. Murzynski, Structure and properties of AlCrN coatings deposited using cathodic arc evaporation, Coatings 10 (793) (Aug. 2020) 1–21, https://doi.org/10.3390/COATINGS10080793.

[11] A. Persson, J. Bergström, C. Burman, S. Hogmark, Influence of deposition temperature and time during PVD coating of CrN on corrosive wear in liquid aluminium, Surf. Coating. Technol. 146–147 (2001) 42–47, https://doi.org/10.1016/S0257-8972(01)01366-4.

[12] K. Valleti, et al., Influence of substrate temperature and bias voltage on properties of chromium nitride thin films deposited by cylindrical cathodic arc deposition influence of substrate temperature and bias voltage on properties of chromium nitride thin films deposited by, J. Vac. Sci. Technol. A Vacuum, Surfaces, Film. 51515 (2011) (2011) 1–7, https://doi.org/10.1116/1.3625234.

[13] K. Taweesup, P. Visuttipitukul, N. Yongvanich, G. Lothongkum, Corrosion behavior of Ti-Cr-N coatings on tool steel substrates prepared using DC magnetron sputtering at low growth temperatures, Surf. Coating. Technol. 358 (May 2018) (2019) 732–740, https://doi.org/10.1016/j.surfcoat.2018.11.082.

[14] D.M. Mattox, Handbook of Physical Vapor Deposition (PVD) Processing, Elsevier Science & Technology Books, 2007, https://doi.org/10.1016/c2009-0-18800-1.

[15] M. Muhammed, M. Javidani, M. Heidari, T. Levasseur, M. Jahazi, Effect of substrate roughness on the tribological performance of AlTiN/AlTiCrN-Coated A8 tool steel, Metall. Mater. Trans. A (Oct. 2025), https://doi.org/10.1007/s11661-025-08013-x.

[16] C.A. Schneider, W.S. Rasband, K.W. Eliceiri, NIH image to ImageJ: 25 years of image analysis, Nat. Methods 9 (7) (2012) 671–675, https://doi.org/10.1038/nmeth.2089.

[17] ASTM G65-04, Standard Test Method for Measuring Abrasion Using the Dry Sand/Rubber Wheel Apparatus, ASTM International, West Conshohocken, PA, Dec. 01, 2010, https://doi.org/10.1520/G0065-04R10.

[18] S. Wu, et al., Effect of C doping on structure and properties of TiAlCrN coatings by filter cathode vacuum arc deposition, Vacuum 201 (2022) 111093, https://doi.org/10.1016/j.vacuum.2022.111093.

[19] E. Poorqasemi, O. Abootalebi, M. Peikari, F. Haqdar, Investigating accuracy of the Tafel extrapolation method in HCl solutions, Corros. Sci. 51 (5) (2009) 1043–1054, https://doi.org/10.1016/j.corsci.2009.03.001.

[20] A. Gilewicz, et al., Comparative investigations of alcrn coatings formed by cathodic arc evaporation under different nitrogen pressure or arc current, Materials 14 (2) (Jan. 2021) 1–20, https://doi.org/10.3390/ma14020304.

[21] Y. Xu, K. Chen, S. Wang, C. Pan, S. Chen, Ti0·33Al0.67 cathode surface modifications and the effect on the mechanical and electrochemical properties of AlTiN coating, Vacuum 131 (2016) 97–105, https://doi.org/10.1016/j.vacuum.2016.05.016.

[22] A. Ostadi, S.H. Hosseini, M.E. Fordoei, The effect of temperature and roughness of the substrate surface on the microstructure and adhesion strength of EB-PVD ZrO2-%8wtY2O3 coating, Ceram. Int. 46 (2) (2020) 2287–2293, https://doi.org/10.1016/j.ceramint.2019.09.217.

[23] T.B.T. To, V.B. de Sousa, F.D.A. Aarão Reis, Thin film growth models with long surface diffusion lengths, Phys. A Stat. Mech. its Appl. 511 (Dec. 2018) 240–250, https://doi.org/10.1016/j.physa.2018.07.024.

[24] R.L. Boxman, S. Goldsmith, Macroparticle contamination in cathodic arc coatings: generation, transport and control, Surf. Coating. Technol. 52 (1) (1992) 39–50, https://doi.org/10.1016/0257-8972(92)90369-L.

[25] A. Anders, Approaches to rid cathodic arc plasmas of macro- and nanoparticles: a review, Surf. Coating. Technol. (1999) 319–330, https://doi.org/10.1016/S0257-8972(99)00460-0.

[26] T. Nojit, P. Visuttipitukul, K. Taweesup, Thermal oxidation resistance of quaternary TiAlCrN coatings prepared with cathodic arc evaporation, J. Australas. Ceram. Soc. 57 (4) (2021) 1209–1218, https://doi.org/10.1007/s41779-021-00617-x.

[27] M. Danek, F. Fernandes, A. Cavaleiro, T. Polcar, Influence of Cr additions on the structure and oxidation resistance of multilayered TiAlCrN films, Surf. Coating. Technol. 313 (2017) 158–167, https://doi.org/10.1016/j.surfcoat.2017.01.053.

[28] Y. Kong, X. Tian, C. Gong, P.K. Chu, Enhancement of toughness and wear resistance by CrN/CrCN multilayered coatings for wood processing, Surf. Coating. Technol. 344 (2018) 204–213, https://doi.org/10.1016/j.surfcoat.2018.03.027.

[29] M. Lahouij, N. Jaghar, O. Abegunde, H. Larhlimi, M. Makha, J. Alami, Structural, mechanical, tribological, and electrochemical behavior of Ti1−xAlxN coatings deposited by high-power impulse magnetron sputtering from a single Ti/Al target, J. Mater. Eng. Perform. (2024), https://doi.org/10.1007/s11665-024-09640-y.

[30] A. Vaitkus, et al., A workflow for deriving chemical entities from crystallographic data and its application to the crystallography open database, J. Cheminf. 15 (1) (2023) 1–15, https://doi.org/10.1186/s13321-023-00780-2.

[31] B.D. Cullity, S.R. Stock, Elements of X-ray diffraction, Phys. Today 10 (3) (1957) 50.

[32] B. Gui, et al., Microstructure and properties of TiAlCrN ceramic coatings deposited by hybrid HiPIMS/DC magnetron co-sputtering, Ceram. Int. 47 (6) (2021) 8175–8183, https://doi.org/10.1016/j.ceramint.2020.11.175.

[33] K. Bobzin, C. Kalscheuer, M. Carlet, D.C. Hoffmann, T. Bergs, L. Uhlmann, Low-temperature physical vapor deposition TiAlCrSiN coated high-speed steel: Comparison between shot-peened and polished substrate condition, Adv. Eng. Mater. 24 (9) (2022), https://doi.org/10.1002/adem.202200099.

[34] L.B. Freund, R. Hull, On the Dodson-Tsao excess stress for glide of a threading dislocation in a strained epitaxial layer, J. Appl. Phys. 71 (4) (1992) 2054–2056, https://doi.org/10.1063/1.351154.

[35] Y. Vengesa, A. Fattah-alhosseini, H. Elmkhah, O. Imantalab, Influence of post-deposition annealing temperature on morphological, mechanical and electrochemical properties of CrN/CrAlN multilayer coating deposited by cathodic arc evaporation- physical vapor deposition process, Surf. Coating. Technol. 432 (Feb) (2022), https://doi.org/10.1016/j.surfcoat.2022.128090.

[36] D. Özkan, et al., Effects of ceramic-based CrN, TiN, and AlCrN interlayers on wear and friction behaviors of AlTiSiN+TiSiN PVD coatings, Ceram. Int. 47 (14) (Jul. 2021) 20077–20089, https://doi.org/10.1016/j.ceramint.2021.04.015.

[37] S.A. Jesuraj, P. Kuppusami, T. Dharini, P. Panda, D. Devapal, Effect of substrate temperature on microstructure and nanomechanical properties of Gd2Zr2O7 coatings prepared by EB-PVD technique, Ceram. Int. 44 (15) (2018) 18164–18172, https://doi.org/10.1016/j.ceramint.2018.07.024.

[38] ASTM E2546-15, Standard Practice for Instrumented Indentation Testing, 2015, https://doi.org/10.1520/E2546-15.

[39] A. Nicholls, Confidence limits, error bars and method comparison in molecular modeling. Part 2: comparing methods, J. Comput. Aided Mol. Des. 30 (2) (2016) 103–126, https://doi.org/10.1007/s10822-016-9904-5.

[40] V. Malau, S. Subagyo, Supriyanto, Effects of heat treatment and titanium nitride (TiN) coating deposited by sputtering technique PVD on duylos 2510 tool steel substrate, Appl. Mech. Mater. 493 (2014) 666–671. https://dx.doi.org/10.4028/www.scientific.net/AMM.493.666.

[41] W. Jiang, D. Wu, Q. Zhang, M. Li, W. Liu, Effect of tempering time on the microstructure and properties of martensitic stainless steel, Metals 14 (3) (2024), https://doi.org/10.3390/met14030322.

[42] M.C.C. de Sá e Benevi Moraes, C.N. Elias, J. Duailibi Filho, L.G. de Oliveira, Mechanical properties of alumina-zirconia composites for ceramic abutments, Mater. Res. 7 (4) (Dec. 2004) 643–649, https://doi.org/10.1590/S1516-14392004000400021.

[43] F. Sansoz, X. Ke, Hall–Petch strengthening limit through partially active segregation in nanocrystalline Ag-Cu alloys, Acta Mater. 225 (2022) 117560, https://doi.org/10.1016/j.actamat.2021.117560.

[44] Y. Zhao, et al., Dislocation motion in plastic deformation of nano polycrystalline metal materials: a phase field crystal method study, Adv. Compos. Hybrid Mater. 5 (3) (2022) 2546–2556, https://doi.org/10.1007/s42114-022-00522-2.

[45] L.A. Dobrzański, L.W. Zukowska, J. Mikuła, K. Gołombek, D. Pakuła, M. Pancielejko, Structure and mechanical properties of gradient PVD coatings, J. Mater. Process. Technol. 201 (1–3) (2008) 310–314, https://doi.org/10.1016/j.jmatprotec.2007.11.283.

[46] S.C. Lee, W.Y. Ho, F.D. Lai, Effect of substrate surface roughness on the characteristics of CrN hard film, Mater. Chem. Phys. 43 (3) (1996) 266–273, https://doi.org/10.1016/0254-0584(95)01636-9.

[47] Y. Zhang, et al., Effect of SiC and TiC content on microstructure and wear behavior of Ni-based composite coating manufactured by laser cladding on Ti–6Al–4V, Wear 552–553 (May) (2024) 205431, https://doi.org/10.1016/j.wear.2024.205431.

[48] M.D. Michel, F.C. Serbena, C.M. Lepienski, Effect of temperature on hardness and indentation cracking of fused silica, J. Non-Cryst. Solids 352 (32–35) (2006) 3550–3555, https://doi.org/10.1016/j.jnoncrysol.2006.02.113.

[49] J.L. Mo, M.H. Zhu, A. Leyland, A. Matthews, Impact wear and abrasion resistance of CrN, AlCrN and AlTiN PVD coatings, Surf. Coating. Technol. 215 (Jan. 2013) 170–177, https://doi.org/10.1016/j.surfcoat.2012.08.077.

[50] B. Porankiewicz, A method to evaluate the chemical properties of particleboard to anticipate and minimize cutting tool wear, Wood Sci. Technol. 37 (1) (2003) 47–58, https://doi.org/10.1007/s00226-003-0166-8.

[51] I.M. Hutchings, P. Shipway, in: Tribology: Friction and Wear of Engineering Materials, second ed., Butterworth-Heinemann, 2017.

[52] Y. Chen, et al., The synergy of V and Si on the microstructure, tribological and oxidation properties of AlCrN based coatings, Surf. Coating. Technol. 412 (Apr) (2021), https://doi.org/10.1016/j.surfcoat.2021.127082.

[53] Y. Yang, Y.F. Cheng, Electrolytic deposition of Ni-Co-SiC nano-coating for erosion-enhanced corrosion of carbon steel pipes in oilsand slurry, Surf. Coating. Technol. 205 (10) (2011) 3198–3204, https://doi.org/10.1016/j.surfcoat.2010.11.035.

[54] S. Bilgin, O. Güler, Ü. Alver, F. Erdemir, M. Aslan, A. Çanakçı, Effect of TiN, TiAlCN, AlCrN, and AlTiN ceramic coatings on corrosion behavior of tungsten carbide tool, J. Australas. Ceram. Soc. 57 (2021) 263–273, https://doi.org/10.1007/s41779-020-00532-7/Published.

[55] Z.A. Fazel, H. Elmkhah, A. Fattah-Alhosseini, K. Babaei, M. Meghdari, Comparing electrochemical behavior of applied CrN/TiN nanoscale multilayer and TiN single-layer coatings deposited by CAE-PVD method, J. Asian Ceram. Soc. 8 (2) (Apr. 2020) 510–518, https://doi.org/10.1080/21870764.2020.1756065.

[56] A.H. Khalaf, B. Lin, Z. Bo, Y. Xiao, A.N. Abdalla, J. Tang, Corrosion rate prediction and inhibitor optimization for L80-1 steel and alloyed materials using response

surface methodology, Surf. Sci. Technol. 3 (1) (2025), https://doi.org/10.1007/s44251-025-00086-5.
[57] P. Kalliotiura, Potential Use of Thermally Sprayed Coatings in Hydrogen Conditions, Tampere University, 2024 [Online]. Available: https://trepo.tuni.fi/bitstream/handle/10024/161084/KalliotiuraPentti.pdf;jsessionid=003F0A5C098CCFE0C2576816D4F972D9?sequence=2.
[58] Y. Zhang, et al., Research on the initial corrosion behavior of A100 steel in salt fog-SO2environment, RSC Adv. 16 (6) (2026) 5309–5324, https://doi.org/10.1039/d5ra08480f.
[59] B. Warcholinski, et al., Effect of nitrogen pressure and substrate bias voltage on the properties of Al–Cr–B–N coatings deposited using cathodic arc evaporation, Tribol. Int. 154 (2021) 106744, https://doi.org/10.1016/j.triboint.2020.106744.
[60] M. Scholl, Abrasive wear of titanium nitride coatings, Wear 203–204 (96) (1997) 57–64, https://doi.org/10.1016/S0043-1648(96)07408-X.
[61] B. Warcholinski, A. Gilewicz, P. Myslinski, E. Dobruchowska, D. Murzynski, T. A. Kuznetsova, Effect of silicon concentration on the properties of Al-Cr-Si-N coatings deposited using cathodic arc evaporation, Materials 13 (21) (Nov. 2020) 1–22, https://doi.org/10.3390/ma13214717.
[62] N.E. Beliardouh, K. Bouzid, C. Nouveau, B. Tlili, M.J. Walock, Tribological and electrochemical performances of Cr/CrN and Cr/CrN/CrAlN multilayr coatings deposited by RF magnetron sputtering, Tribol. Int. 82 (2015) 443–452.